

# AN INFRARED THROUGH RADIO STUDY OF THE PROPERTIES AND EVOLUTION OF IRDC CLUMPS

CARA BATTERSBY<sup>1,2</sup>, JOHN BALLY<sup>1</sup>, JAMES M. JACKSON<sup>2</sup>, ADAM GINSBURG<sup>1</sup>, YANCY L. SHIRLEY<sup>3</sup>, WAYNE SCHLINGMAN<sup>3</sup>,  
JASON GLENN<sup>1</sup>

*Draft version October 31, 2018*

## ABSTRACT

We examine the physical properties and evolutionary stages of a sample of 17 clumps within 8 Infrared Dark Clouds (IRDCs) by combining existing infrared, millimeter, and radio data with new Bolocam Galactic Plane Survey (BGPS) 1.1 mm data, VLA radio continuum data, and HHT dense gas (HCO<sup>+</sup> and N<sub>2</sub>H<sup>+</sup>) spectroscopic data. We combine literature studies of star formation tracers and dust temperatures within IRDCs with our search for ultra-compact (UC) H II regions to discuss a possible evolutionary sequence for IRDC clumps. In addition, we perform an analysis of mass tracers in IRDCs and find that 8  $\mu$ m extinction masses and 1.1 mm Bolocam Galactic Plane Survey (BGPS) masses are complementary mass tracers in IRDCs except for the most active clumps (notably those containing UCH II regions), for which both mass tracers suffer biases. We find that the measured virial masses in IRDC clumps are uniformly higher than the measured dust continuum masses on the scale of  $\sim 1$  pc. We use <sup>13</sup>CO, HCO<sup>+</sup>, and N<sub>2</sub>H<sup>+</sup> to study the molecular gas properties of IRDCs and do not see any evidence of chemical differentiation between hot and cold clumps on the scale of  $\sim 1$  pc. However, both HCO<sup>+</sup> and N<sub>2</sub>H<sup>+</sup> are brighter in active clumps, due to an increase in temperature and/or density. We report the identification of four UCH II regions embedded within IRDC clumps and find that UCH II regions are associated with bright ( $\gtrsim 1$  Jy) 24  $\mu$ m point sources, and that the brightest UCH II regions are associated with “diffuse red clumps” (an extended enhancement at 8  $\mu$ m). The broad stages of the discussed evolutionary sequence (from a quiescent clump to an embedded H II region) are supported by literature dust temperature estimates; however, no sequential nature can be inferred between the individual star formation tracers.

*Subject headings:* dust, extinction - ISM: clouds - stars: formation and pre-main sequence

## 1. INTRODUCTION

Despite their profound impact on the galactic environment and enrichment, the protostellar evolution (and birth) of massive stars ( $M > 8 M_{\odot}$ ) remains elusive. Direct observations of the earliest evolutionary stages of massive stars is a challenging task. Massive stars evolve more quickly, are more rare, and consequently farther away on average than their low-mass counterparts. In addition, massive stars, once formed, quickly heat and ionize their environment, disrupting their natal molecular cloud. Much like their low-mass counterparts, massive stars are thought to form in cold, dense molecular clouds. Massive stars seem to form predominantly in clusters (Lada & Lada 2003; de Wit et al. 2005) and therefore, their natal molecular cloud should be more massive and denser than the natal clouds of isolated low-mass stars. Infrared Dark Clouds (IRDCs) have been proposed to be the progenitors of massive stars and their host clusters (Egan et al. 1998; Carey et al. 1998; Rathborne et al. 2006).

IRDCs were identified as dark extinction features against the bright mid-infrared galactic plane with the MSX and ISO space satellites (Egan et al. 1998; Perault et al. 1996; Omont et al. 2003). IRDCs were catalogued from the MSX 8  $\mu$ m data by Simon et al. (2006a) and from the GLIMPSE 8  $\mu$ m data more recently by Peretto & Fuller (2009). The strong continuum extinc-

tion and lack of infrared emission by these clouds belie their cold temperatures and high column densities. Previous studies have confirmed that these clouds are indeed cold ( $T < 25$  K) and dense ( $n_H > 10^5$  cm<sup>-3</sup>) (Egan et al. 1998; Carey et al. 1998, 2000). More recently, studies have found kinematic distances to these clouds and determined that their masses lie in the range of  $10^2$  to  $10^4 M_{\odot}$  (Rathborne et al. 2006). Ragan et al. (2009) find a clump mass spectra (over the range of clump masses from 30 to 3000  $M_{\odot}$ ) in IRDCs with a slope of about  $1.76 \pm 0.05$ .

There is compelling evidence to suggest that IRDCs are the cold, dense precursors to stellar clusters, and thus massive stars. Millimeter continuum maps show extended cold dust emission, matching the morphology of the IRDCs and surrounding compact clumps<sup>1</sup>. These clumps fall into two categories: active and quiescent. The active clumps are characterized by some or all of the following: 1) luminous, embedded 24  $\mu$ m emission, 2) “green fuzzies,” (Chambers et al. 2009) an extended 4.5  $\mu$ m enhancement believed to be caused by shocked H<sub>2</sub>, thus indicative of outflows (also known as Extended Green Objects, EGOs Cyganowski et al. 2008), 3) maser emission, and 4) ultra-compact (UC) H II regions. A quiescent clump is characterized as a cold, dense millimeter peak with none of the aforementioned signs of active star

<sup>1</sup> Center for Astrophysics and Space Astronomy – University of Colorado Boulder

<sup>2</sup> Institute for Astrophysical Research – Boston University

<sup>3</sup> Steward Observatory – University of Arizona

<sup>1</sup> In this paper, we use the term “core” to describe a small, dense object within an IRDC clump, with a size of order 0.05 pc which will likely form a single star or stellar system, “clump” to describe a dense object within an IRDC with a size of order  $\sim 1$  pc and a mass  $10^2$  -  $10^3 M_{\odot}$ , and “cloud” for an IRDC which has a size scale of order 10 pc, and a mass of order  $10^3$  -  $10^4 M_{\odot}$ .

formation. It is believed that the active clumps are currently forming stars while the quiescent clumps are at an earlier stage of star formation: the cold, dense precursor before the star has “turned on.”

IRDCs are the densest clumps and filaments embedded within Giant Molecular Clouds (GMCs: Simon et al. 2006b) with the favorable viewing condition of being on the near-side of a bright mid-IR background. They are preferentially found toward the Galaxy’s largest star-forming region, the 5 kpc ring. IRDCs have typical sizes  $D \sim 1\text{-}10$  pc, densities  $n_H \gtrsim 10^4$  cm $^{-3}$ , and masses  $M \sim 10^2\text{-}10^4 M_\odot$  (Rathborne et al. 2006). IRDCs are dense condensations embedded within GMCs ( $D \sim 50$  pc,  $n \sim 10^2$  cm $^{-3}$ , and  $M \sim 10^5\text{-}10^6 M_\odot$ ) and are typically larger and more massive than Bok Globules ( $D \sim 0.1\text{-}2$  pc,  $n \sim 10^3\text{-}10^4$  cm $^{-3}$ , and  $M \sim 1\text{-}100 M_\odot$ ; Rathborne et al. 2006). Many have argued that stars can form anywhere in a GMC, but that the confining pressure and column density of an IRDC are required for the formation of clusters and massive stars (e.g. McKee & Tan 2003). The formation mechanism of an IRDC within a GMC is not well understood. Perhaps it is simply the gravitational collapse of a high-density perturbation in a GMC left on its own for many free-fall times. Alternatively, IRDCs may be the result of triggered collapse in a high-pressure environment, such as a cloud-cloud collision, or the dynamic force from a bubble, such as an H II region, wind, supernova, or superbubble. Converging flows are another possible trigger for the collapse of an IRDC from part of a GMC. An IRDC, once formed, has the properties of cluster-forming clumps (Lada & Lada 2003) with the exception that IRDCs are much colder (10 - 20 K). Do these IRDC clumps fragment into cores which evolve in isolation or do the resulting cores undergo competitive accretion? This is a central question in massive star formation (Zinnecker & Yorke 2007; McKee & Ostriker 2007).

This paper explores a sample of 17 IRDC clumps embedded within 8 IRDCs. We compare various mass tracers in IRDCs, distinguish active and quiescent clumps, and discuss a possible evolutionary sequence. This paper is organized as follows. In §2, we describe the source selection and observations. In §3, we present mass estimation techniques, their results, and an analysis of the systematic errors involved. These masses are compared in §4.1. In §4.2 we compare the 8  $\mu\text{m}$  dust extinction with the BGPS 1.1 mm dust emission. In §4.3 we address whether or not the IRDC clumps are bound, and in §4.4 we compare the molecular line tracers. In §4.5, we discuss the radio continuum sources and stellar type limits for the UCH II regions found and in §4.6 we discuss star formation activity in the clumps. In §5, we discuss a possible evolutionary sequence for IRDC clumps. §6 is a summary of our conclusions. Appendix A includes a discussion of each IRDC as well as images of each source with all the data used in the paper.

## 2. SOURCE SELECTION AND DATA

### 2.1. Source Selection

In this paper, we investigate a sample of 17 IRDC clumps embedded within 8 IRDCs. These were selected from the MSX dark cloud catalog (Simon et al. 2006a), and from the previous work of Rathborne et al.

(2006), who selected the 38 highest contrast IRDCs from the dark cloud catalog with known kinematic distances. These 38 IRDCs, therefore, are among the darkest and densest in the catalog by Simon et al. (2006a). From this subset, and based upon the work by Chambers et al. (2009), we selected mostly active clumps, with a few quiescent clumps for comparison. Our sample consists of 9 active, 4 intermediate, and 4 quiescent clumps. We mostly selected clumps with signs of active star formation, motivated by our UCH II region survey, as this would maximize our detection rate. We included a few quiescent clumps in our sample for comparison, although no UCH II regions were expected in the quiescent clumps. Our sample of IRDC clumps is a subset of the darkest, most active IRDC clumps in the First Galactic Quadrant ( $0 \leq l \leq 90^\circ$ ). In a sample of 106 IRDC clumps, Chambers et al. (2009) find that 65% are quiescent and 35% are active clumps. We quantify the star-forming activity by four criteria: 1) an embedded 24  $\mu\text{m}$  point source, 2) “green fuzzies,” (Chambers et al. 2009) an extended 4.5  $\mu\text{m}$  enhancement believed to be caused by shocked H $_2$ , thus indicative of outflows (also known as Extended Green Objects, EGOs Cyganowski et al. 2008), 3) H $_2$ O or CH $_3$ OH maser emission, and 4) Ultra-compact (UC) H II regions. We assign the designation “active” to clumps which have three or four of these signs of star formation, which means that each “active” clump has either an H II region or at least two outflow tracers and a 24  $\mu\text{m}$  point source, and is actively forming stars. The designation “intermediate” is for clumps which exhibit one or two signs of active star formation. These clumps, therefore, may have only shock/outflow signatures or a 24  $\mu\text{m}$  point source. We reserve the designation “quiescent” for clumps with no signs of active star formation.

Selection of the clump positions from the sample discussed above required simply that there be an IR-dark feature, which can be near but not coincident with an IR-bright region, which has corresponding millimeter emission. The exact clump positions were selected by eye based on the above criteria and the overlap with existing data. While the exact clump positions were not selected by stringent thresholds, visual inspection of the images verifies that the sample accurately represents the IRDCs. The clump positions and the closest millimeter clump, as identified by Rathborne et al. (2006), are given in Table 1.

### 2.2. Observations & Data Description

For this study, we examine a sample of 17 IRDC clumps within 8 IRDCs. We utilize existing and new data to determine the physical properties and evolutionary stages of these clumps. A summary of the data used is found in Table 2.

#### 2.2.1. Mid-Infrared Data

We utilize mid-IR data taken as part of the Galactic Legacy Infrared Mid-Plane Survey Extraordinaire (GLIMPSE; Benjamin et al. 2003) and 24  $\mu\text{m}$  data taken as part of the MIPS GAL survey (Carey et al. 2009). Extinction at 8  $\mu\text{m}$  gives an independent mass estimate, the 4.5  $\mu\text{m}$  band determines the presence of “green fuzzies,” and embedded stellar sources appear at 8 and 24  $\mu\text{m}$ . We

TABLE 1  
 IRDC CLUMP POSITIONS

IRDC Name <sup>a</sup>	Glimpse Clump Name	Bolocat <sup>b</sup> Clump Name	Closest MAMBO <sup>c</sup> Clump Name	R.A. (J2000)	DEC. (J2000)
MSXDC G022.35+00.41	GLM1	2860	MM1	18:30:24.2	-09:10:38.9
	GLM2	2858	MM3	18:30:37.6	-09:12:54.1
MSXDC G023.60+00.00	GLM1	3125	MM2	18:34:21.3	-08:18:07.5
	GLM2	3132	MM7	18:34:20.6	-08:17:21.7
MSXDC G024.33+00.11	GLM1	3284	MM1	18:35:08.1	-07:35:01.9
	GLM2	3282	MM4	18:35:19.1	-07:37:19.7
MSXDC G024.60+00.08	GLM1	3382	MM2	18:35:35.8	-07:18:22.2
	GLM2	3383	MM1	18:35:39.9	-07:18:46.0
MSXDC G028.23-00.19	GLM1	3923	MM1	18:43:30.3	-04:13:03.7
MSXDC G028.37+00.07	GLM1	3946	MM14	18:42:53.4	-04:02:23.8
	GLM2	3939	MM4	18:42:50.6	-04:03:16.9
	GLM3	3942	MM6	18:42:48.9	-04:02:05.4
	GLM4	3955	MM1	18:42:52.5	-03:59:48.1
MSXDC G028.53-00.25	GLM1	3998	MM2	18:44:16.1	-04:00:09.9
MSXDC G034.43+00.24	GLM1	5373	MM1	18:53:18.0	+01:25:24.9
	GLM2	5373	MM2	18:53:18.4	+01:24:51.3
	GLM3	5385	MM3	18:53:19.6	+01:28:24.6

<sup>a</sup> from the MSX dark cloud catalog by Simon et al. (2006a). For the remainder of the paper we drop the MSXDC prefix.

<sup>b</sup> BGPS 1.1 mm clump source catalog, Bolocat, number (Rosolowsky et al. 2010)

<sup>c</sup> from Rathborne et al. (2006)

 TABLE 2  
 SUMMARY OF OBSERVATIONS

Data	$\lambda$	Beam FWHM	$1\sigma$ Sensitivity
GLIMPSE	3.6 $\mu\text{m}$	1.7"	0.3 MJy/Sr <sup>a</sup>
GLIMPSE	4.5 $\mu\text{m}$	1.7"	0.3 MJy/Sr
GLIMPSE	5.8 $\mu\text{m}$	1.9"	0.7 MJy/Sr
GLIMPSE	8.0 $\mu\text{m}$	1.9"	0.6 MJy/Sr
MIPSGAL	24 $\mu\text{m}$	6"	0.67 mJy
HHT	1.12 mm <sup>b</sup>	28"	0.04 K
HHT	1.07 mm <sup>b</sup>	27"	0.04 K
GRS	2.86 mm <sup>b</sup>	46"	0.27 K
VLA	3.6 cm	2.8 x 2.4"	0.05 mJy/beam
IRAM	1.2 mm	11"	10 mJy/beam
BGPS	1.1 mm	33"	30 mJy/beam

<sup>a</sup> GLIMPSE raw  $1\sigma$  surface brightness sensitivities from Reach et al. (2006)

<sup>b</sup>  $\text{HCO}^+$  J = 3-2,  $\text{N}_2\text{H}^+$  J = 3-2, and  $^{13}\text{CO}$  J = 1-0 respectively. For  $\text{HCO}^+$  and  $\text{N}_2\text{H}^+$ , 0.04 K is the  $1\sigma$  sensitivity per 1.1 km  $\text{s}^{-1}$  channel and for  $^{13}\text{CO}$ , 0.27 K is the  $1\sigma$  sensitivity per 0.21 km  $\text{s}^{-1}$  channel

utilize the ‘‘green fuzzy’’ (extended 4.5  $\mu\text{m}$  emission, indicative of shocks) catalog by Chambers et al. (2009), as well as their 24  $\mu\text{m}$  point source identification and  $\text{H}_2\text{O}$  and  $\text{CH}_3\text{OH}$  maser survey.

### 2.2.2. Millimeter Continuum Dust Emission

The millimeter continuum data traces the cold dust within the IRDCs and gives cloud and clump mass estimates, as well as the locations of compact clumps within the IRDCs. We utilize 1.2 mm data obtained at the Institut de Radioastronomie Millimétrique (IRAM) 30 m telescope with MAMBO II from Rathborne et al. (2006). The FWHM angular resolution of each element in the array is 11", with a separation between each element of 20". The final ( $1\sigma$ ) r.m.s. noise level in these maps is  $\sim 10$  mJy/beam.

We present additional millimeter data taken with Bolocam (Glenn et al. 2003) on the Caltech Submillimeter

Observatory (CSO) 10 m diameter telescope at 1.1 mm as part of the Bolocam Galactic Plane Survey, BGPS v1.0<sup>1</sup> (Aguirre et al. 2010; Rosolowsky et al. 2010). Bolocam is a 144-element (of which 115 are working) bolometer array arranged on a uniform hexagonal grid. Each bolometer has an effective FWHM of 33" and the array field of view is 7'.5. The data were taken with a 45 GHz bandwidth filter centered at 268 GHz, which excludes the bright 230 GHz J=2-1 CO line. The data were reduced using a custom pipeline created for the BGPS using the methods described in Aguirre et al. (2010). The dominant source of noise at these wavelengths, the atmospheric component, is removed using Principle Component Analysis (PCA). This cleaning process limits the spatial scale to which we are sensitive to between about 30" to 400". The final ( $1\sigma$ ) r.m.s. noise level in these

<sup>1</sup> <http://irsa.ipac.caltech.edu/data/BOLOCAM-GPS/>

maps is  $\sim 30$  mJy/beam.

### 2.2.3. $^{13}\text{CO}$ $J=1-0$ Molecular Gas Tracer

As a tracer of column density, radial velocities, and for spectral line comparison, we include  $^{13}\text{CO}$   $J=1-0$  data taken as part of the Boston University-Five College Radio Astronomy Observatory Galactic Ring Survey (BU-FCRAO GRS; Jackson et al. 2006). These data was obtained from 1998-2005 using the single sideband focal plane array receiver, SEcond QUabbin Optical Imaging Array (SEQUOIA) on the FCRAO 14 meter. At a central frequency of 110.2 GHz, the beam FWHM is  $46''$  and the spectral resolution is  $0.21 \text{ km s}^{-1}$ . We correct the  $^{13}\text{CO}$  antenna temperatures for the main beam efficiency of 0.48 through the expression  $T_{mb} = T_A^*/\eta_{mb}$ . The  $1 \sigma$  sensitivity in the GRS data is about 0.27 K.

### 2.2.4. VLA Radio Continuum Data

In order to unambiguously determine which massive clumps have entered the main sequence, we used the Very Large Array (VLA) in New Mexico to look for thermal bremsstrahlung from newly formed H II regions. We observed a total of twelve positions over eight IRDCs in the X band in the C configuration in the spring 2008. We observed single channel continuum in the X band, centered at 3.6 cm with a bandwidth of 50 MHz. We performed flux calibrations on 3C286 and phase calibrations on 1832-105 and 1851+005. The data were reduced using standard continuum interferometric techniques in the AIPS software package. The primary beam is  $5.4'$ , and the highest resolution element is about  $2.8 \times 2.4''$ . This translates to 0.06 (0.10) pc resolution for the nearest (farthest) clump. We had a total of three six-hour sessions. We observed each source three times per session, changing the order each night to obtain good coverage of the u-v plane. We integrated for an hour total on each source achieving a  $1 \sigma$  r.m.s. flux density of  $\sim 0.05$  mJy/beam.

### 2.2.5. $\text{HCO}^+$ and $\text{N}_2\text{H}^+$ Dense Molecular Gas Tracers

To determine the radial velocities of the clumps and their molecular structure, we probe the dense molecular gas using the  $J=3-2$  transitions of  $\text{HCO}^+$  and  $\text{N}_2\text{H}^+$  (rest frequencies of 267.5576190 and 279.5117010 GHz respectively). Using the 1 mm dual polarization ALMA-prototype Sideband Separating Receiver on the Heinrich Hertz Telescope (HHT), we observed  $\text{HCO}^+$  and  $\text{N}_2\text{H}^+$  simultaneously with  $1.1 \text{ km s}^{-1}$  spectral resolution and  $28''$  and  $27''$  spatial resolution ( $\Theta_{FWHM}$ ). We performed two minute position-switched observations on the seventeen IRDC clumps, which gave us an r.m.s. noise level of about 0.04 K. We On-the-Fly mapped (see Mangum et al. 2007) the five most compelling clouds in both molecular lines simultaneously. We mapped the clouds, scanning twice in RA and twice in DEC with a row spacing of  $10''$  at a scan speed of  $5''$  per second. The separate maps were offset by about  $4''$ . We pointed, focused, and calibrated on Jupiter every 2 or 3 hours when it was available, otherwise, we pointed and focused on G34.3+0.15. We used S140 as a check of the line position and intensity about every two hours, and also to determine the Vertical / Horizontal Polarization ratio

(Vpol/Hpol) and the typical sideband rejection measurement. Typical sideband rejection between the USB and LSB for each polarization was between 13 and 15 dB. We correct for the main beam efficiency of 0.75 and the ratio  $V\text{pol}/H\text{pol} = 1.1$  in our data reduction.

The single spectra were reduced using standard procedures in the Gildas CLASS<sup>1</sup> software package. The baselines were removed, the horizontal polarization was multiplied by the Vpol/Hpol scaling factor and then co-added. We then corrected for the main beam efficiency, giving us  $T_{mb}$ . The On-the-Fly maps were reduced using some custom and shared software in the Gildas CLASS package. The same procedure as above was followed for each individual spectrum. The spectra were then interpolated onto a regular grid using a Gaussian tapered Bessel function (Reiter, M. private communication; Mangum et al. 2007).

## 3. MASS ESTIMATES

Mass is one of the most fundamental physical properties necessary to understand the nature of a region. However, there is no perfect tracer of mass. Molecular line mass tracers, such as  $^{13}\text{CO}$  may suffer from depletion, optical depth effects or varying excitation conditions. Virial masses are only reliable in the idealized case of a gravitationally bound object in virial equilibrium, where the line is broadened simply by virialized motion. An extinction mass is limited by *a priori* knowledge of the foreground and background radiation field, and the absorption properties of the obscuring dust. Dust continuum masses are thought to be a promising tracer of cold, dense environments, but are also sensitive to varying dust temperature, emissivity, and grain properties. The distance estimate plays a significant role in the mass uncertainty via the assumption of a Galactic rotation curve, and the ambiguity associated with the velocity scatter of objects at any given distance. Each of these tracers is also affected by the statistical uncertainties in each measured quantity. For this study, we find that the systematic uncertainties far outweigh the statistical uncertainties and include only estimates of the systematic uncertainty in §3.6.

A minimization and characterization of systematics is vital for a fair comparison of IRDC mass tracers. For this reason, we have convolved the extinction and MAMBO 1.2 mm maps to the BGPS resolution using a Gaussian kernel with a width given by  $\sigma_{conv} = \sqrt{\sigma_{bgps}^2 - \sigma_{org}^2}$  where  $\sigma_{org}$  is the original width of the beam that is being convolved. Each mass is then retrieved within a circular aperture with the equivalent area of the BGPS Gaussian beam,

$$r_{eff} = \frac{\Theta_{fwhm}}{2\sqrt{\ln 2}} = 19.81'' \quad (1)$$

This allows us to compare these mass estimates independent of beam filling factors and beam or source sizes. Where possible, we also calculate the total cloud mass, the mass within the elliptical aperture used to define the extent of the IRDC for extinction mapping (see Figure 1). The line widths used to determine the virial masses were achieved from single pointings of  $\text{HCO}^+$  on the HHT, which has an effective beam FWHM of about  $28''$  at these

<sup>1</sup> <http://www.iram.fr/IRAMFR/GILDAS>

TABLE 3  
 PROPERTIES OF THE IRDC CLUMPS

Clump	$V_{LSR}$ (km s <sup>-1</sup> )	$\Delta V$ (km s <sup>-1</sup> )	Distance (kpc)	$f_{fore}^a$	$\tau_{8\mu m}$	<sup>13</sup> CO	HCO <sup>+</sup>	N <sub>2</sub> H <sup>+</sup>	Integrated Intensity (K km s <sup>-1</sup> )			
						Peak T <sub>MB</sub> (K)	Peak T <sub>MB</sub> (K)	Peak T <sub>MB</sub> (K)	<sup>13</sup> CO	HCO <sup>+</sup>	N <sub>2</sub> H <sup>+</sup>	
G022.35+00.41												
GLM1	52.4	3.4	3.6	0.14	1.3	5.4	1.9	1.2	8.6	8.0	5.4	
GLM2	83.9	3.4	4.8	0.23	0.7	8.2	0.8	0.3	18.0	2.5	0.8	
G023.60+00.00												
GLM1	53.3	6.7	3.6	0.14	0.7	4.3	1.1	1.3	12.0	7.1	6.0	
GLM2	53.4	4.5	3.6	0.14	0.8	4.7	0.6	0.6	12.1	2.4	2.4	
G024.33+00.11												
GLM1	113.4	6.7	5.9	0.33	0.7	6.8	1.6	3.4	30.0	12.1	20.0	
GLM2	114.1	5.6	5.9	0.33	0.7	5.2	0.5	0.3	26.1	2.8	1.8	
G024.60+00.08												
GLM1	114.7	3.4	6.0	0.33	1.3	4.6	0.6	0.5	7.7	2.2	2.2	
GLM2	53.0	5.6	3.5	0.14	1.2	5.6	1.5	1.0	14.1	8.7	5.5	
G028.23-00.19												
GLM1	79.7	4.5	4.6	0.23	1.5	5.8	0.3	0.3	28.4	1.7	1.5	
G028.37+00.07												
GLM1	78.8	5.6	4.5	0.23	2.6	4.7	1.1	1.2	21.0	5.9	4.1	
GLM2	77.9	4.5	4.5	0.23	2.5	6.3	2.1	1.6	29.0	9.9	6.8	
GLM3	78.9	2.2	4.5	0.23	1.8	4.9	1.2	1.3	24.7	4.9	5.2	
GLM4	76.7	6.7	4.4	0.23	1.4	7.0	1.4	1.8	25.9	7.4	12.3	
G028.53-00.25												
GLM1	86.2	5.6	4.9	0.26	0.4	6.6	0.4	0.2	22.3	1.7	1.1	
G034.43+00.24												
GLM1	58.0	6.7	3.6	0.18	0.7	6.7	5.4	6.4	23.9	37.4	37.0	
GLM2	57.5	6.7	3.6	0.18	0.4	8.5	6.4	6.2	30.0	46.0	34.6	
GLM3	59.5	5.6	3.7	0.18	0.9	7.2	2.9	2.5	18.4	18.0	11.7	

<sup>a</sup> The fraction of foreground emission along the line of sight, see §3.2

frequencies, similar to the BGPS beam. In most cases the radius used to determine the virial mass (the “virial radius”) is very similar in size to the circular aperture radius, so these are fair comparisons in terms of source size. The <sup>13</sup>CO masses were retrieved from single GRS pointings, with an effective FWHM of about 46”. The mass in this case is estimated over a greater area than the other techniques, so it will include a wider region and more emission, which we consider when making mass comparisons. We chose not to degrade the resolution of the other maps past the 33” for the BGPS beam to match the <sup>13</sup>CO beam as the <sup>13</sup>CO is considered a secondary mass estimator, and is included only for comparison.

We explain below the techniques for achieving the different mass estimates and the estimated systematic uncertainty in Section 3.6. We then compare these mass estimates and discuss their differences and similarities.

### 3.1. Distance Estimates

CO is the second most abundant molecule in interstellar space. It is found nearly everywhere, including IRDCs. In these dense, cold environments, however, even the less abundant <sup>13</sup>CO can become optically thick and can deplete onto dust grains (e.g. Tafalla et al. 2002). HCO<sup>+</sup> and N<sub>2</sub>H<sup>+</sup> are less abundant than <sup>13</sup>CO and therefore become optically thick at higher columns of H<sub>2</sub>. The critical density is also much higher,  $3.5 \times 10^6 \text{ cm}^{-3}$  and  $3.0 \times 10^6 \text{ cm}^{-3}$  for the J=3-2 transitions of HCO<sup>+</sup> and N<sub>2</sub>H<sup>+</sup> respectively, compared with  $1.9 \times 10^3 \text{ cm}^{-3}$  for <sup>13</sup>CO J=1-0. Therefore, there is typically only one HCO<sup>+</sup> or N<sub>2</sub>H<sup>+</sup> source along a given line-of-sight, which can then be confidently associated with the dense IRDC, as opposed to CO which is often seen at many velocities along a given line-of-sight through the

Galactic plane. For this reason, we use the HCO<sup>+</sup> velocity to determine the kinematic distance to each IRDC. A kinematic distance had already been determined to each of these objects using <sup>13</sup>CO morphology matching by Simon et al. (2006b), however, we find that in the confused inner Galaxy, morphology matching can misassign distances. Two clouds of our sample of eight (G022.35+00.41 and G024.60+00.08) are spatially adjacent clumps along the line-of-sight at very different distances, as opposed to a contiguous object as found by Simon et al. (2006b).

Distances were estimated kinematically using the HCO<sup>+</sup> clump velocities and the rotation curve of Reid et al. (2009), determined with trigonometric parallaxes and proper motions of masers using the VLBA and Japanese VERA project. In the First Galactic quadrant, a radial velocity can correspond to two possible distances, a problem known as the “Kinematic Distance Ambiguity”. Since IRDCs are perceived as dark extinction features against the Galactic background, it is assumed that all IRDCs are located at the near kinematic distance. If we assume an average velocity scatter at any given distance of about 5% (about 5-10 km s<sup>-1</sup>), this translates to an approximate distance uncertainty of 20%. The distances, line-widths, and observed properties of the clumps are listed in Table 3.

### 3.2. Extinction Masses

The mid-IR extinction by IRDCs provides a powerful way to obtain an independent measure of their column density. We restrict our analysis of extinction to the 8  $\mu\text{m}$  band of GLIMPSE, as this band is dominated by emission from the diffuse ISM, rather than stellar sources. We apply the extinction mapping method put forth by Butler & Tan (2009). In brief, this method esti-

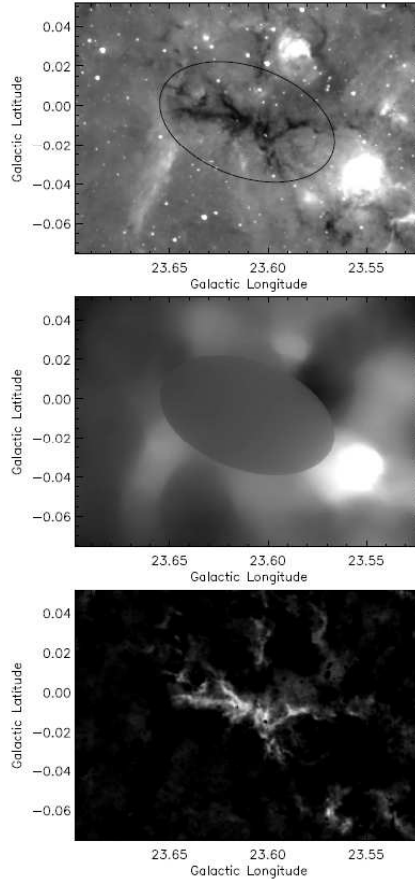


FIG. 1.— G023.60+00.00 Top:  $8\ \mu\text{m}$  GLIMPSE image with ellipse approximating the extent of the IRDC. This image represents the values of  $I_{\nu 1,obs}$  in Equation 5. Middle: Circularly median filtered  $8\ \mu\text{m}$  image with the points in the ellipse determined by interpolation from outside so they are not skewed by the IRDC. This is a proxy for the diffuse Galactic background,  $I_{\nu 0,obs}$  in Equation 4 Bottom: Final surface density map in units of  $\text{g cm}^{-2}$

mates the Galactic background and foreground emission, finds the optical depth required to produce the observed extinction feature, assumes a dust opacity, and finally extracts the gas mass surface density. Our application of this method is described below.

To accurately map the extinction, we need to estimate the intensity of radiation behind the cloud of interest,  $I_{\nu 0}$ , and the radiation in front of the cloud,  $I_{\nu 1}$ . Assuming no emission from the cloud itself at these wavelengths, we have

$$I_{\nu 1} = I_{\nu 0} e^{-\tau_{\nu}} \quad (2)$$

where  $\tau_{\nu} = \kappa_{\nu} \Sigma$ ,  $\kappa_{\nu}$  is the dust opacity, and  $\Sigma$  is the surface mass density. We adopt a value of  $\kappa_{8\mu\text{m}} = 11.7\ \text{cm}^2\ \text{g}^{-1}$ , following the analysis of Butler & Tan (2009) (they adopt a value of  $7.5\ \text{cm}^2\ \text{g}^{-1}$  as they use a gas-to-dust ratio of 156, rather than the value of 100 used in this paper). This value is closest to the model of Ossenkopf & Henning (1994) of thin ice mantles that have undergone coagulation for  $10^5$  years at a density of  $n_{\text{H}_2} \sim 10^6\ \text{cm}^{-3}$ , which is a reasonable model for the cold, dense environment of an IRDC. This expression assumes that the dust opacity remains constant along the line-of-sight, which may not be true. However, most of the extinction arises from the coldest, densest parts of the cloud. In the less dense regions, the opacity may vary by up to a factor of two, but we assume that the majority of the extinction is caused by the coldest, dens-

est regions of the cloud, which are well-characterized by the adopted value of  $\kappa_{8\mu\text{m}}$ .

Before proceeding with the background determination, we must first estimate the fraction of emission from dust in the foreground. We assume that the Galactic distribution of hot dust (in the Galactic midplane) is given by the Galactic surface density of OB associations (McKee & Williams 1997)

$$\Sigma_{OB} \propto e^{-R/H_R} \quad (3)$$

where  $R$  is the Galactocentric radius (in kpc) and  $H_R = 3.5$  kpc is the Galactic radial scale length. We then integrate the column of dust from the sun (Reid et al. 2009, at  $R_0 = 8.4$  kpc from the Galactic center) to the cloud, and the column of dust along the same line of sight, from the Sun out to a Galactocentric radius of 16 kpc (beyond which there is a negligible contribution to the dust emission). The ratio of the column to the cloud over the column out to 16 kpc is called the ‘Foreground Intensity Ratio’,  $f_{fore}$ ; the fraction of emission along the line-of-sight that is from the foreground. Thus, the true radiation behind the cloud,  $I_{\nu 0}$ , determined from that observed,  $I_{\nu 0,obs}$ , is given by

$$I_{\nu 0} = (1 - f_{fore}) I_{\nu 0,obs} \quad (4)$$

and the true radiation in front of the cloud,  $I_{\nu 1}$ , deter-

mined from that observed,  $I_{\nu 1,obs}$  is given by

$$I_{\nu 1} = I_{\nu 1,obs} - f_{fore} I_{\nu 0,obs}. \quad (5)$$

Butler & Tan (2009) note that  $f_{fore}$  is uncertain because of the inevitable small-scale variations in the Galactic background and the fact that the regions surrounding the IRDC are likely to be embedded in the same GMC that hosts the IRDC. This leads to a higher extinction of the integrated Galactic background, creating a tendency to underestimate  $f_{fore}$  and thus  $\Sigma$ .

An upper limit for  $f_{fore}$  is provided by the minimum flux at  $8 \mu\text{m}$  divided by the average background. This value would be  $f_{fore}$  if the cloud were totally opaque at  $8 \mu\text{m}$ . This upper limit is about 2 times higher in most cases, except in G028.37+00.07, where it is about the same. The remainder of the IRDCs may or may not be optically thick at  $8 \mu\text{m}$ , however, the good correlation (see Figure 2) with BGPS 1.1 mm masses (which is almost certainly optically thin) is an indication that many of the IRDCs are still optically thin at  $8 \mu\text{m}$ .

For the purpose of estimating the Galactic background, we employ the more accurate small-scale median filter (SMF) approach from Butler & Tan (2009). This approach is designed to capture the small-scale variations in the background, without altering the estimate by the darkness of the IRDC itself. Thus, we first exclude an ellipse approximating the size and shape of the IRDC from the filtering process (Figure 1, top). To smooth the data, we first remove the high-end tail of the distribution (all points greater than twice the mode) which is mostly due to stars. We then perform a circular spatial median filter at each point, i.e. we compute the median of all the data in a circle around a given point, and that becomes the smoothed data value at that point. A reasonable size for the filter was empirically determined to be a radius of one arcminute. This smoothed map is our estimate of the diffuse Galactic background. We then estimate the ‘background’ inside the ellipse by taking the average of the smoothed data values from outside the ellipse, weighted by the inverse square of their distance from the point. This is depicted in the middle frame of Figure 1. This image is now our estimate of  $I_{\nu 0,obs}$ , and our original image is  $I_{\nu 1,obs}$ . Using Equation 6 we then create a surface density map, shown in Figure 1 in the bottom panel.

$$\Sigma = -\frac{1}{\kappa_{\nu}} \ln \left[ \frac{I_{\nu 1,obs} - f_{fore} I_{\nu 0,obs}}{(1 - f_{fore}) I_{\nu 0,obs}} \right] \quad (6)$$

There is an additional correction that must be taken into account for quantities derived from extended sources in the IRAC data. Scattering from extended sources within the IRAC array systemically increases the measured surface brightness. For a uniformly distributed extended source, this scattering increases the measured surface brightness by about  $\sim 30\%$  at  $8 \mu\text{m}$  (S. Carey, private communication and <http://ssc.spitzer.caltech.edu/irac/iracinstrumenthandbook/33/>). This means that the *measured* background ( $I_{\nu 0,obs}$ ) is systematically brighter than the *true* background, which we will call  $T_0$  for simplicity. Where  $s = 0.3$ , the scattering correction, the *true* background is given by  $T_0 = (1 + s) I_{\nu 0,obs}$ . The *measured* foreground ( $I_{\nu 1,obs}$ ) is also contaminated by scattered light from the background, so the *true* foreground ( $T_1$ ) is given

by  $T_1 = I_{\nu 1,obs} + s I_{\nu 0,obs}$ . Plugging these values into Equation 6, simplifying, and writing the surface density in terms of our measured quantities, our final expression for the surface density is:

$$\Sigma = -\frac{1}{\kappa_{\nu}} \ln \left[ \frac{(s + 1) I_{\nu 1,obs} - (s + f) f_{fore} I_{\nu 0,obs}}{(1 - f_{fore}) I_{\nu 0,obs}} \right] \quad (7)$$

Using distances determined from the  $\text{HCO}^+$  velocities and the Reid et al. (2009) rotation curve, we are then able to sum the surface density over the BGPS beam-sized apertures to obtain the mass (see Table 4 and Figure 2) in the clump. The extinction masses for the clumps range from 60 to 620  $M_{\odot}$  and from 1200 to 26,020  $M_{\odot}$  for the whole IRDC.

### 3.3. Dust Continuum Masses

Obtaining mass estimates of IRDCs with molecular lines is often problematic due to high column densities and molecular freezeout onto dust grains. The cold dust emission, however, as observed in the millimeter, provides more reliable mass estimates as it is optically thin and does not deplete. We use both the 1.2 mm and 1.1 mm dust continuum emission from MAMBO and the BGPS, to achieve isothermal mass estimates using the expression

$$M = \frac{S_{\nu} D^2}{\kappa_{\nu} B_{\nu}(T)} \quad (8)$$

where  $S_{\nu}$  is the source flux density,  $D$  is the distance,  $\kappa_{\nu}$  is the dust opacity and  $B_{\nu}(T)$  is the Planck function at dust temperature,  $T$ . We adopt a value of  $\kappa_{1.1mm} = 0.0114 \text{ cm}^2 \text{ g}^{-1}$  from Enoch et al. (2006), in which we have assumed a gas-to-dust ratio of 100. This opacity is consistent with the Ossenkopf & Henning (1994) model used for the  $8 \mu\text{m}$  opacity in the extinction masses. The mass equation reduces to

$$M_{1.1mm} = 14.32 (e^{13.0/T} - 1) \left( \frac{S_{\nu}}{1 \text{ Jy}} \right) \left( \frac{D}{1 \text{ kpc}} \right)^2 M_{\odot} \quad (9)$$

$$M_{1.2mm} = 20.82 (e^{12.0/T} - 1) \left( \frac{S_{\nu}}{1 \text{ Jy}} \right) \left( \frac{D}{1 \text{ kpc}} \right)^2 M_{\odot}. \quad (10)$$

We assume a dust temperature  $T = 15 \text{ K}$ . We can also find the column density of  $\text{H}_2$ , as given by

$$N(\text{H}_2) = \frac{S_{\nu}}{\Omega_B \kappa_{\nu} B_{\nu}(T) \mu_{\text{H}_2} m_{\text{H}}} \quad (11)$$

$$N(\text{H}_2)_{1.1mm} = 2.20 \times 10^{22} (e^{13.0/T} - 1) S_{\nu} \text{ cm}^{-2} \quad (12)$$

$$N(\text{H}_2)_{1.2mm} = 3.20 \times 10^{22} (e^{12.0/T} - 1) S_{\nu} \text{ cm}^{-2} \quad (13)$$

where  $\Omega_B$  is the beam size,  $\mu_{\text{H}_2}$  is the mean molecular weight for which we adopt a value of  $\mu_{\text{H}_2} = 2.8$  (Kauffmann et al. 2008). The dust continuum masses and column densities are listed in Table 4. The total BGPS 1.1 mm cloud masses range from 1200 to 13,000  $M_{\odot}$  while the clump masses range from 80 to 1100  $M_{\odot}$ .

TABLE 4  
 MASS COMPARISON

Clump <sup>a</sup>	Aperture		Column Density in 33" BGPS Beam			<sup>13</sup> CO	Mass inside 33" BGPS Beam			<sup>13</sup> CO	Virial Mass (M <sub>⊙</sub> )	R <sub>vir</sub> (pc)
	Size <sup>b</sup> (pc)	Extinction	BGPS (10 <sup>22</sup> cm <sup>-2</sup> )	MAMBO	Column	Extinction (M <sub>⊙</sub> )	BGPS (M <sub>⊙</sub> )	MAMBO (M <sub>⊙</sub> )	Mass (M <sub>⊙</sub> )			
G022.35+00.41												
GLM1	0.7	2.3	1.1	2.9	0.4	190	95	250	70	340	0.2	
GLM2	0.9	1.3	1.2	1.4	0.9	200	180	210	240	2300	1.3	
G023.60+00.00	2.9 x 1.8					1200	1200	1800				
GLM1	0.7	1.2	1.7	3.0	0.6	100	140	250	100	1800	0.3	
GLM2	0.7	1.4	1.0	1.7	0.6	120	81	140	90	660	0.2	
G024.33+00.11	6.0 x 8.0					12010	13000	14000				
GLM1	1.1	1.4	4.8	8.6	1.5	310	1200	1950	610	2500	0.4	
GLM2	1.1	1.3	1.4	1.9	1.3	300	310	440	530	3100	0.7	
G024.60+00.08												
GLM1	1.2	2.4	1.3	2.3	0.4	560	310	550	160	850	0.5	
GLM2	0.7	2.1	1.6	3.2	0.7	170	130	260	100	1000	0.2	
G028.23-00.19	5.2 x 3.3					5520	3700	1900				
GLM1	0.9	2.8	1.4	2.0	1.4	380	190	270	350	910	0.3	
G028.37+00.07	5.8 x 4.5					26020	13000	18000				
GLM1	0.9	4.7	1.6	3.0	1.0	620	220	400	250	2100	0.5	
GLM2	0.9	4.6	2.2	3.9	1.4	610	290	520	350	330	0.1	
GLM3	0.9	3.3	1.4	2.6	1.2	430	190	340	290	370	0.5	
GLM4	0.9	2.6	5.3	10.3	1.3	350	700	1400	290	4400	0.7	
G028.53-00.25	7.3 x 4.6					4800	7300	11000				
GLM1	0.9	0.7	1.6	3.5	1.1	110	250	540	310	3500	0.8	
G034.43+00.24	6.9 x 2.3					5550	7500	14000				
GLM1	0.7	1.3	10.1	17.8	1.2	110	850	1500	180	3000	0.4	
GLM2	0.7	0.7	9.3	15.9	1.5	60	790	1300	230	2500	0.4	
GLM3	0.7	1.7	2.2	3.9	0.9	140	190	330	150	1700	0.4	

<sup>a</sup> The clump names are from the MSX dark cloud catalog (Simon et al. 2006a), and have had the “MSXDC” prefix removed

<sup>b</sup> For the clumps, the aperture size is the physical size of the 40" diameter circular BGPS aperture. For the cloud, it is the physical major and minor axes of the ellipse approximating the extent of the IRDC.

### 3.4. Virial Masses

The molecular line width of these objects provides an independent measure of mass. The virial mass is based on the assumption that the object is gravitationally bound and in virial equilibrium. Therefore, the virial mass estimate, in combination with other mass estimates, may allow discussion of whether or not the clump is bound and virialized. For a density profile of  $\rho(r) = r^{-\alpha}$ , the virial mass is given by

$$M_{\text{vir}} = 3 \left[ \frac{5 - 2\alpha}{3 - \alpha} \right] \frac{R\sigma^2}{G} \quad (14)$$

where  $\sigma$  is the line-of-sight velocity dispersion,  $R$  is the virial radius, and  $G$  is the gravitational constant. We adopt a spectral index of  $\alpha = 1.8$ , which was found to be the mean in a sample of 31 massive star-forming regions by Mueller et al. (2002) with a standard deviation of 0.4. However, this spectral index was derived from a sample of “active” clumps, so this is an added source of uncertainty for quiescent clumps. We do not include a correction for ellipticity, as these clumps are compact enough to be well-approximated by spheres. This expression reduces to

$$M_{\text{vir}} = 147 \left( \frac{R}{1 \text{ pc}} \right) \left( \frac{\Delta v_{\text{fwhm}}}{1 \text{ km s}^{-1}} \right)^2 M_{\odot} \quad (15)$$

where  $R$  is the virial radius and  $\Delta v_{\text{fwhm}}$  is the line width at half maximum. In order to determine the best estimate for the virial radius, a two-dimensional circular Gaussian was fit to each BGPS clump. The Gaussian fit

was then deconvolved from the BGPS beam. The effective radius (see Eq. 1) of the deconvolved Gaussian fit is the virial radius, given in Table 4. In this study, we assign a virial ‘radius’ to a Gaussian beam which is likely convolved with a power-law distribution of cores within the beam. The meaning of the virial ‘radius’ in this case is tricky as the deconvolved source size can vary by up to a factor of two depending on the slope of the power law distribution of sources within the beam (Shirley et al. 2003, Figure 16). However, this method is consistent between the clumps in our sample, and is a reasonable proxy for the size scale of the diffuse emission.

We use the FWHM of the HCO<sup>+</sup> line for the virial masses presented here. Using the N<sub>2</sub>H<sup>+</sup> line width instead does not change the results qualitatively, as the two tracers provide consistent line widths across different activity levels. N<sub>2</sub>H<sup>+</sup> has been shown to be well correlated with submm dust column in starless cores (Tafalla et al. 2002; Wyrowski et al. 2000), meaning that these virial masses are most likely based on the same material which is producing the dust continuum. The virial masses of the clumps were found to range from 330 to 4400 M<sub>⊙</sub>.

### 3.5. <sup>13</sup>CO Masses

<sup>13</sup>CO is commonly used to estimate the column density and mass of molecular clouds in the Galaxy. However, due to depletion onto dust grains (Tafalla et al. 2002) and optical depth effects in cold, dense environments, <sup>13</sup>CO is not the most reliable tracer of column in IRDCs. While there is good morphological agreement between the 8 μm extinction and the <sup>13</sup>CO toward the dense clumps in IRDCs, Du & Yang (2008) show that <sup>13</sup>CO



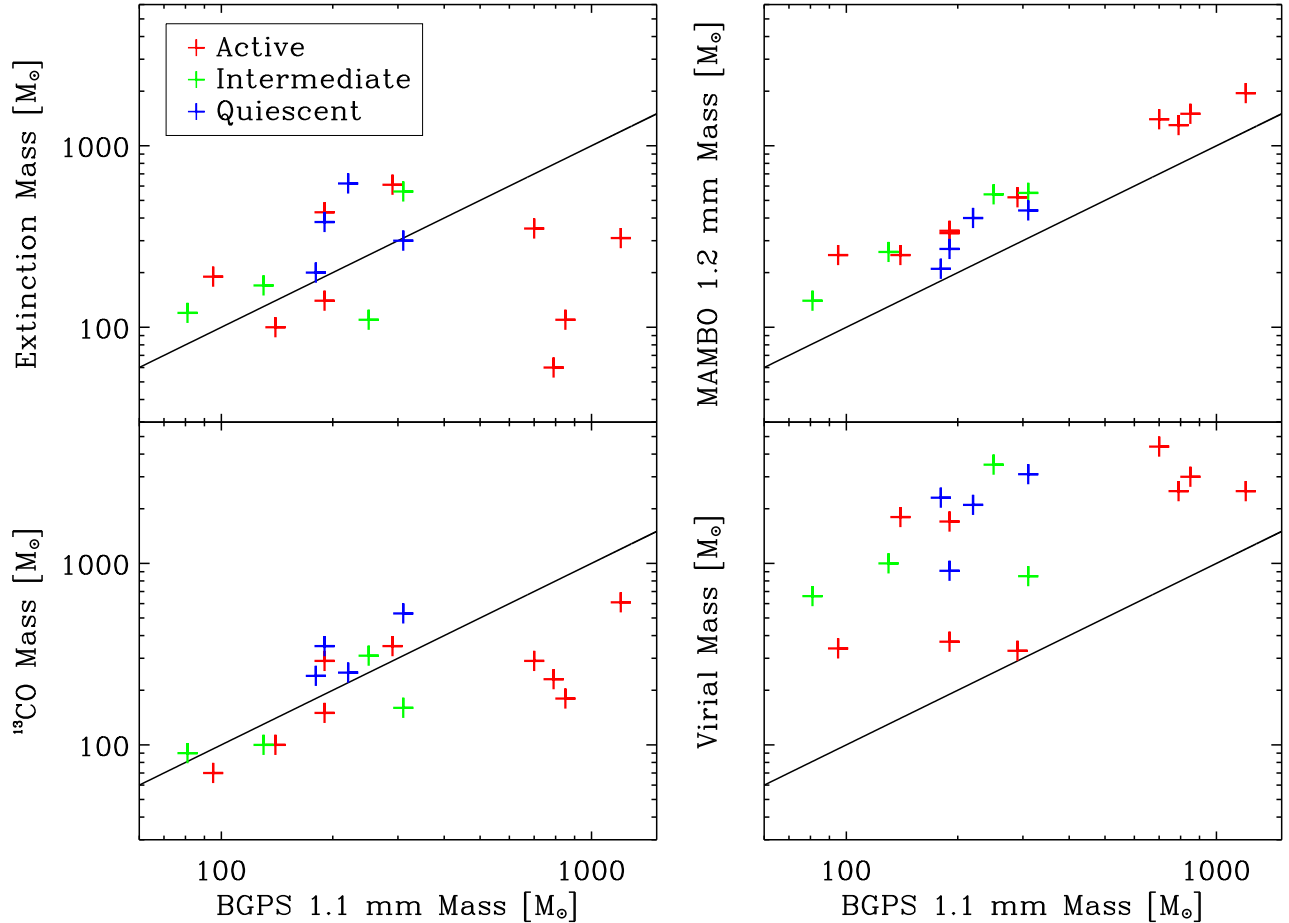


FIG. 2.— A comparison of mass estimates for the clumps (see Table 4). The line drawn has a slope of 1, representing equality. The red crosses are “active” clumps, the green are “intermediate,” and the blue are “quiescent.” Note that the four highest BGPS 1.1 mm mass objects (where there is significant discrepancy) are all associated with UCH II Regions.

is optically thick toward many IRDCs, so we caution the reader that these tracers are probably not probing to the same depth in dense IRDC clumps. Du & Yang (2008) also demonstrate that typical excitation temperatures of  $^{13}\text{CO}$  in IRDCs are of the order of  $\sim 10$  K. This indicates that the  $^{13}\text{CO}$  is at the very least tracing to some depth in the cold, dense region of the clump, however the  $^{13}\text{CO}$  is also tracing the surrounding GMC and IRDC envelope. We include column density and mass estimates from  $^{13}\text{CO}$  as a secondary mass tracer, and as a comparison to other tracers. In the optically thin, thermalized limit, the  $^{13}\text{CO}$  column density is given by

$$N(\text{H}_2) = \frac{8\pi k\nu^3 X_{^{13}\text{CO}}}{3c^3 h B_J A_{10}} (1 - e^{-h\nu/kT_{ex}})^{-1} \int T_{mb} dv \quad (16)$$

where  $\nu$  is the frequency of the  $^{13}\text{CO}$  J=1-0 transition,  $A_{10}$  is the Einstein A coefficient of  $^{13}\text{CO}$  from state J=1 to J=0,  $T_{ex}$  is the excitation temperature,  $B_J$  is the rotation constant, and  $X_{^{13}\text{CO}}$  is the fraction of  $^{13}\text{CO}$  to  $\text{H}_2$ . We adopt a value of  $^{12}\text{CO} / ^{13}\text{CO}$  of 58 from Lucas & Liszt (1998), and a value of  $^{12}\text{CO} / \text{H}_2$  of  $10^{-4}$ , a value of 55.101038 GHz for  $B_J$ , and standard NIST values for all constants and spectral transition values. This

expression then reduces to

$$N(\text{H}_2) = 1.45 \times 10^{17} \frac{\int T_{mb} dv}{1 - e^{-5.29/T}} \text{cm}^{-2} \quad (17)$$

This column density can then be converted to a mass via

$$M = N(\text{H}_2) \mu_{\text{H}_2} m_H A \quad (18)$$

where  $\mu_{\text{H}_2}$  is the mean molecular weight of  $\text{H}_2$ ,  $m_H$  is the mass of hydrogen, and  $A$  is the physical area over which the mass is summed. We adopt a value of  $\mu_{\text{H}_2} = 2.8$  (Kauffmann et al. 2008). This expression reduces to

$$M = 5.00 \times 10^{-25} N(\text{H}_2) \left( \frac{A}{1 \text{ arcsec}^2} \right) \left( \frac{D}{1 \text{ kpc}} \right)^2 M_\odot \quad (19)$$

where  $A$  is the area in  $\text{arcsec}^2$ , over which the mass is summed, and  $D$  is the distance in kpc. The  $^{13}\text{CO}$  clump masses range from 70 to 610  $M_\odot$ .

### 3.6. Mass Error Analysis

For this study, we find that the systematic uncertainties far outweigh the statistical uncertainties. We present below our estimated systematic uncertainties and the method used to derive them.

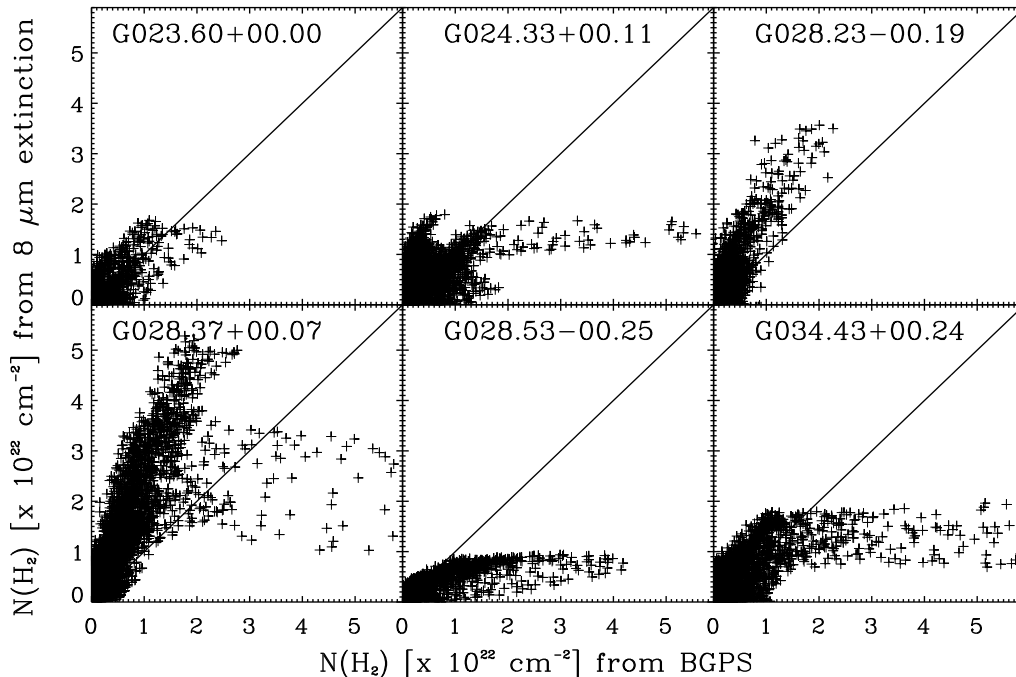


FIG. 3.— A pixel-by-pixel comparison of  $8\ \mu\text{m}$  extinction column density vs. BGPS 1.1 mm column density for points within the IRDC ellipse. The black line is the 1:1 line.

We assign each variable in the mass equation (Eqns. 6, 9, 10, 15, and 19) a fractional uncertainty, perform a Monte-Carlo simulation randomly drawing the variables from a Gaussian distribution, and report the 68% confidence interval over which the mass varies. Since we have reason to believe that each of the variables is centered at our adopted value, we assign each variable a randomly populated Gaussian distribution, centered at the adopted value and with a width such that 99.7% of the points are within the lower and upper bounds of the fractional uncertainty. For example, we assign an uncertainty to the distance of 20%. Therefore, for each run, we randomly sample the distance value from a Gaussian which is centered at the adopted value and has a width such that 99.7% of the points lie between 0.8 and 1.2 times the adopted distance value. For each mass estimate, we ran at least  $10^7$  points in the simulation. We note that several of the mass probability distributions below are asymmetric. To be consistent with the literature, we present the mass estimates at the adopted variable values (which is equal to the mean of the mass probability distribution), but note that this is not the same as the median or most probable value of the distribution. The 68% confidence intervals were drawn from the median of the distribution outwards. We divide the high and low mass ends of the confidence interval by the mass at the peak of the distribution to achieve the asymmetric 68% confidence intervals.

The dominant sources of uncertainty in the extinction mass estimate are the background and foreground estimates, the scattering coefficient, as well as the distance, opacity, and  $f_{\text{fore}}$ . We find that typical fluctuations in the  $8\ \mu\text{m}$  emission near IRDCs, on the scale of the IRDCs, is around 40%. This background fluctuation is the best measure we have for how much the background behind the IRDC will vary from what we measure, so we assign

a 40% uncertainty to the background estimate. In calculating the foreground uncertainty, we assign the same 40% uncertainty to the measured background and an additional 50% uncertainty to the value of  $f_{\text{fore}}$ . We include a 15% uncertainty in the value of the scattering coefficient as the color variation is about 5% and not being able to characterize the spatial dependency of the scattering has about a 10-15% effect (S. Carey, private communication). We also include a 20% uncertainty in the distance determination (as discussed in Section 3.1) and factor of two uncertainty in the value of the opacity as recommended by Ossenkopf & Henning (1994). The 68% confidence intervals for the extinction mass are from 80% to 2.2 times the quoted mass.

For the dust continuum (BGPS 1.1 mm and MAMBO 1.2 mm) mass estimates, the dominant uncertainties are the temperature, the flux density, the opacity, and the distance. For both the 1.1 mm and 1.2 mm data, we assign an uncertainty of 50% to the temperature (for most clumps the temperature is between 10-20 K; Dunham et al. 2010), 10% to the flux density (Aguirre et al. 2010), a factor of two uncertainty in the opacity (as above), and 20% to the distance. The 68% confidence intervals for both dust continuum masses are from 80% to 180% of the quoted mass.

The systematic uncertainty associated with the virial mass is difficult to characterize. The basic assumption that the clump is a gravitationally bound object in virial equilibrium introduces an inherent uncertainty that cannot be quantified. Another major uncertainty is the virial radius. The true radius of these clumps is in most cases unknown, so assigning an uncertainty is somewhat questionable. Our typical virial radii are around 0.4 pc and some interferometric millimeter studies of IRDC clumps (e.g Beuther et al. 2005) find sizes of about 0.1 pc. Therefore, we assign an uncertainty of a factor of

4 to the virial radius. The line-width is uncertain by about 20% for these data. These uncertainties give us a 68% confidence interval for the virial masses from 50% to 170% of the quoted value. In cases where the adopted virial radius is off by a wide margin, the virial mass will also be off by that same wide margin (as the calculated mass scales linearly with the adopted virial radius).

The quantifiable systematic uncertainties in the  $^{13}\text{CO}$  mass are the excitation temperature, integrated line intensity, and distance. However, there is a large uncertainty that we are unable to quantify associated with the optical depth, freezeout, excitation conditions, and variable abundance of  $^{13}\text{CO}$  in cold, dense clumps (e.g. Tafalla et al. 2002). These will have the effect of lowering the  $^{13}\text{CO}$  mass and column density estimates. We assign an uncertainty to the excitation temperature of 50% (as above), an uncertainty in the integrated intensity of 20%, and an uncertainty in the distance of 20%. We find that the 68% confidence interval for the  $^{13}\text{CO}$  masses is from 80% to 120% of the quoted mass, neglecting additional uncertainties introduced by optical depth and freezeout effects.

#### 4. ANALYSIS

##### 4.1. Mass Comparison

Given the systematic uncertainties, the agreement between the various mass tracers is reasonable, as shown in Table 4 and Figure 2. All of the mass tracers increase with increasing BGPS 1.1 mm dust continuum mass, except for extinction and  $^{13}\text{CO}$  at the highest BGPS 1.1 mm masses, as these are associated with UCHII Regions (See Table 5). The virial masses are uniformly higher than the BGPS 1.1 mm masses, the ratio of the two ranges from 1.1 to 14.4 with a median of  $6.4 \pm 4.2$ . A detailed comparison of the BGPS 1.1 mm mass with the virial mass is given in §4.3. The MAMBO 1.2 mm masses are also uniformly higher than the BGPS 1.1 mm masses, though not nearly as high as the virial masses. The ratio of MAMBO 1.2 mm to BGPS 1.1 mm masses ranges from 1.2 to 2.6 with a median of  $1.8 \pm 0.3$ . This offset is intrinsic to data taken with MAMBO at 1.2 mm vs. Bolocam at 1.1 mm. The reason for this offset is being investigated by the BGPS team and will be discussed in Aguirre et al. (2010). The  $^{13}\text{CO}$  masses agree surprisingly well with the BGPS 1.1 mm masses, the ratio between the two ranges from 0.2 to 1.9 with an median of  $0.8 \pm 0.5$ . Recall, however, that the  $^{13}\text{CO}$  mass is taken over a  $46''$  beam rather than the  $33''$  effective beam size of the rest, so we are including more of the GMC and the IRDC envelope, and therefore more emission. This means that the true comparable  $^{13}\text{CO}$  mass would be generally *lower* than the BGPS 1.1 mm mass. The agreement between the two is best at lower BGPS 1.1 mm masses. At higher BGPS column there is likely a higher than assumed BGPS temperature, as well as optical depth effects or freezeout of  $^{13}\text{CO}$  at high column densities (Tafalla et al. 2002). The extinction mass and BGPS 1.1 mm mass agree well, except at the highest BGPS 1.1 mm masses ( $M_{\text{BGPS}} > 600 M_{\odot}$ ), where the sources are associated with UCH II Regions. The ratio of extinction to BGPS 1.1 mm mass ranges from 0.1 to 2.8 with an median of  $1.1 \pm 0.8$ . A more detailed comparison of the extinction mass to the BGPS 1.1 mm mass

is given below.

##### 4.2. Dust extinction and emission

The relationship between  $8 \mu\text{m}$  extinction and 1.1 mm dust emission is reasonably good, and where it is not, there is good indication that warm gas/dust due to a hot clump is skewing both extinction and emission measures of mass. Recent dust temperature estimates from Rathborne et al. (2010) corroborate that active clumps are indeed warmer than quiescent/intermediate clumps. The agreement between  $8 \mu\text{m}$  extinction and 1.1 mm dust emission masses is poor in the four highest BGPS 1.1 mm mass sources, which are associated with UCH II Regions. In these regions, the temperature is almost certainly warmer than the assumed 15 K, which contributes to the very large BGPS fluxes. Additionally, the UCH II Region illuminates PAH features in the  $8 \mu\text{m}$  band, boosting the  $8 \mu\text{m}$  flux and reducing the measured extinction mass.

Figure 3 shows the extinction column density vs. BGPS 1.1 mm column density and we note that while the column density derived from extinction and the BGPS 1.1 mm dust continuum generally agree there are some peculiarities. Note that the clumps indicated in Table 4 are only a small portion of what is plotted in Figure 3. Figure 3 plots the entire IRDC, while the table only includes the subsections of the cloud chosen for this study as clumps. In some sources the extinction flattens out as the 1.1 mm column increases, while in others the extinction column is higher than that 1.1 mm column. These indicate a hot clump (with imperfect temperature assumptions for the 1.1 mm dust emission and  $8 \mu\text{m}$  contamination by PAH illumination) and either a cold clump or imperfect foreground/background estimation, respectively. For the individual clumps, the median of the ratio of extinction column to BGPS column is  $1.1 \pm 0.8$  overall,  $0.7 \pm 0.9$  for active clumps,  $1.4 \pm 0.6$  for intermediate clumps and  $2.0 \pm 0.9$  for quiescent clumps. This is in agreement with our assessment that high extinction per 1.1 mm column is characteristic of quiescent clumps, low extinction per 1.1 mm column is characteristic of active clumps, however, there is still a lot of scatter. Though there are some exceptions, in general, dust extinction and emission are well correlated for quiescent/intermediate clumps, but often diverge for active clumps, particularly ones associated with UCHII Regions.

##### 4.3. A Comparison of Virial and Dust Masses

Simple calculations show that the measured virial masses are uniformly higher than the masses measured through other techniques, such as the dust continuum emission. The median of the ratio of the virial mass to the BGPS 1.1 mm mass is  $6.4 \pm 4.2$ , and ranges from 1.1 to 14.4. Interferometric observations (Rathborne et al. 2007, 2008; Wang et al. 2008; Zhang et al. 2009, for more details on specific sources, please see the Appendix) of several of these sources find that most clumps fragment into smaller cores at higher resolution, with sizes of about 0.03 pc or less. Zhang et al. (2009) find that on the scale of  $\sim 0.02$  pc the virial and dust mass estimates agree quite well. On the scale of about 1 pc, we find that the virial masses are much higher than the dust masses. The virial radius required for our measured virial masses to match our measured BGPS 1.1 mm masses ranges from

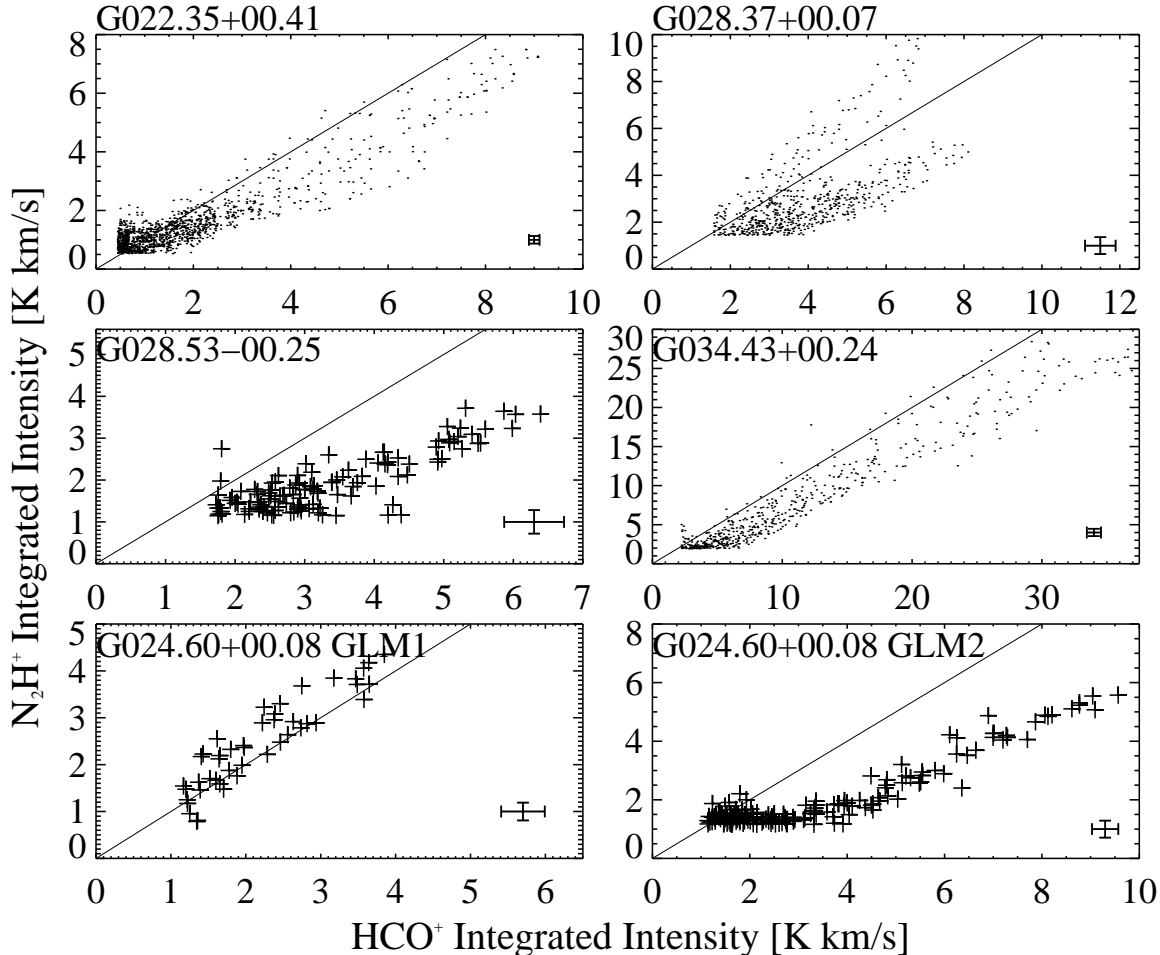


FIG. 4.— Ratio of the integrated intensities of  $\text{N}_2\text{H}^+$  ( $J=3-2$ ) to  $\text{HCO}^+$  ( $J=3-2$ ). Only pixels greater than  $4\sigma$  in  $\text{HCO}^+$  and  $\text{N}_2\text{H}^+$  are shown. This is a pixel-by-pixel comparison of the  $\text{HCO}^+$  and  $\text{N}_2\text{H}^+$  points within the IRDC ellipse. The line drawn has a slope of one representing equality. The point in the lower right corner of each plot represents the approximate  $1\sigma$  error bars for the points in that plot.

0.02 to 0.25 pc with a mean of  $0.09 \pm 0.06$  pc, similar to the interferometric size scales noted above. The information presented is consistent with the picture of small bound cores (about 0.01 pc in size), surrounded by a dense envelope (about 0.1 pc in size) which is also bound, engulfed in a diffuse envelope (size scale of about 1 pc). This dense envelope is where the majority of dense gas is emitting and therefore dominates the line width we measure, while the diffuse envelope extends out to about 1 pc and comprises the extended emission we see in the dust continuum. In this picture, the line widths we measure are primarily from a region that is smaller than the virial radius we assign to it, thus explaining the very large virial to dust mass ratio. Alternatively, if the material producing the large line widths and the dust continuum emission are the same, it is possible that something more than virialized motion (e.g. magnetic fields, turbulence) are playing a role in the line widths or that the clumps are not gravitationally bound, and possibly ram-pressure confined by converging flows (e.g. Heitsch et al. 2008). The question of whether these clouds, clumps, and cores are bound is of great importance in understanding cluster formation.

#### 4.4. A Molecular Line Tracer Comparison

The ratio of  $\text{HCO}^+$  to  $\text{N}_2\text{H}^+$  in clumps of varying activity levels is of special interest, as it is thought that  $\text{HCO}^+$  will trace “hot” clumps while  $\text{N}_2\text{H}^+$  will trace “cold” clumps (Jørgensen et al. 2004).  $\text{HCO}^+$  is created by CO in the gas phase, and will also deplete onto dust grains at cold temperatures, so it should be more abundant in hotter environments.  $\text{N}_2\text{H}^+$ , on the other hand, is destroyed by CO in the gas phase, and should be more abundant in colder environments. Figure 4 is a pixel-by-pixel comparison of  $\text{N}_2\text{H}^+$  to  $\text{HCO}^+$  integrated intensities, and the line is of slope one, representing equality. Throughout the majority of the clouds, the ratio of  $\text{HCO}^+$  to  $\text{N}_2\text{H}^+$  is greater than one. In a few cases (most notably G028.37+00.07), however, the  $\text{N}_2\text{H}^+$  integrated intensity is greater than the  $\text{HCO}^+$ . This is due to a high column of gas and dust, in which  $\text{HCO}^+$  is optically thick, and self-absorbed which lessens the peak (e.g. Figure 15(b)), making  $\text{N}_2\text{H}^+$  brighter by comparison. The general trend is that  $\text{HCO}^+$  and  $\text{N}_2\text{H}^+$  are well correlated and that  $\text{HCO}^+$  is slightly brighter. In Figure 5 we see that our present sample shows no trend between clump activity and the ratio of  $\text{HCO}^+$  to  $\text{N}_2\text{H}^+$ . It is important to note that we are not resolving individual cores, so

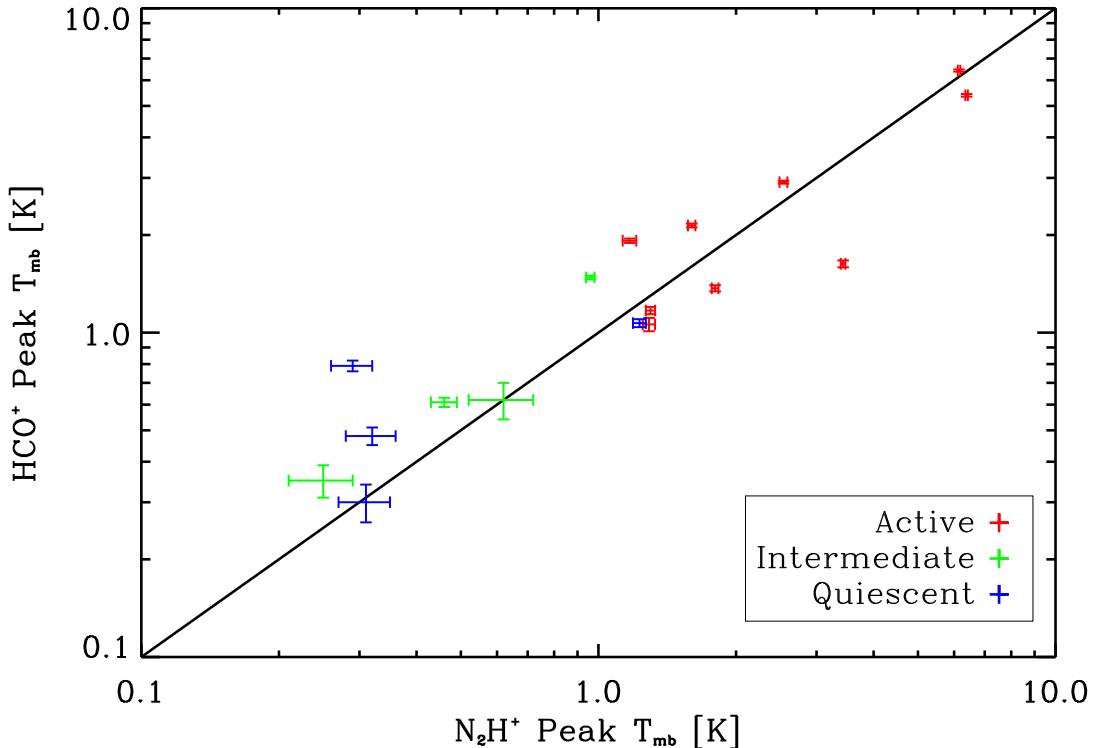


FIG. 5.—  $\text{HCO}^+$  vs.  $\text{N}_2\text{H}^+$  Peak  $T_{\text{mb}}$  on a log-log plot. Red is active clumps, green is intermediate and blue is quiescent (See Table 5). The line drawn has a slope of one, representing equality. Note that there is no noticeable distinction in the ratio of  $\text{HCO}^+$  to  $\text{N}_2\text{H}^+$  for active vs. quiescent clumps, but that active clumps are much brighter in  $\text{HCO}^+$  and  $\text{N}_2\text{H}^+$  than quiescent clumps.

adjacent cores with differing chemistry will result in an average, rather than resembling distinct core chemistries. Additionally, we are comparing line strengths, not abundances.

While we see no evidence for a chemical differentiation between  $\text{HCO}^+$  and  $\text{N}_2\text{H}^+$  on a  $\sim 1$  pc scale between “active” and “quiescent” clumps, we note that active clumps are significantly brighter in  $\text{HCO}^+$  and  $\text{N}_2\text{H}^+$  than intermediate or quiescent clumps. The increased brightness of  $\text{HCO}^+$  and  $\text{N}_2\text{H}^+$  in active clumps could be the result of an increased column density, higher volume density, higher temperature, and/or a larger beam filling factor. We argue that an increase in column is not the primary effect as not all active clumps have higher dust column, yet all active clumps show an increased brightness in  $\text{HCO}^+$  and  $\text{N}_2\text{H}^+$ . The change in filling factor is a possible explanation, however the  $\text{HCO}^+$  and  $\text{N}_2\text{H}^+$  maps show extended emission around all the clumps. Since at the typical density of an IRDC ( $n \sim 10^5 \text{ cm}^{-3}$ ) we are approaching the critical densities of  $\text{HCO}^+$  and  $\text{N}_2\text{H}^+$  (see Daniel et al. 2007), we suggest that the active clumps may have begun to compress and become denser, increasing the intensity of  $\text{HCO}^+$  and  $\text{N}_2\text{H}^+$ . This increase in density is also responsible for the increased optical depth of  $\text{HCO}^+$  in active clumps, as evidenced by the self-absorption of  $\text{HCO}^+$  in some active clumps. Recent dust temperature estimates from Rathborne et al. (2010) suggest that active clumps are warmer, which would also increase the observed brightness of  $\text{HCO}^+$  and  $\text{N}_2\text{H}^+$ . We observe that  $\text{HCO}^+$  and  $\text{N}_2\text{H}^+$  are brighter in active than quiescent clumps and suggest that this is because

the active clumps are either warmer, have higher volume densities, or both.

We also compare the  $\text{HCO}^+$  and  $\text{N}_2\text{H}^+$  peak line intensities with those of  $^{13}\text{CO}$  in Figure 6. As discussed in Section 3.5, while there is good evidence that  $^{13}\text{CO}$  is optically thick toward many of these clumps, we see that it at least traces to some depth in the cold, dense portion of the clump. However, the  $^{13}\text{CO}$  is almost certainly tracing some part of the GMC and IRDC envelope as well. Therefore, we include it as an optically thick comparison point for the dense gas tracers. The  $^{13}\text{CO}$  peak varies very little among the different clump types and shows no noticeable increase with column, again corroborating that it is optically thick. The  $\text{HCO}^+$  and  $\text{N}_2\text{H}^+$  peak temperatures increase somewhat with column density, but most notably with activity level. This means that the active clumps all have much smaller variation in line strength than the quiescent clumps (the line connecting the peak  $T_{\text{mb}}$ ’s is shorter). The variation in line strength among the three tracers can be quantified by the difference between the brightest peak line strength of the three tracers and the weakest peak line strength of the three tracers. The mean of the variation in line strength is  $4.5 \pm 0.8$  for active clumps,  $4.8 \pm 1.1$  for intermediate clumps, and  $5.5 \pm 1.8$  for quiescent clumps. While the numbers are uncertain, the trend is clear, and this is a potentially useful tool for identifying active clumps.

#### 4.5. H II Regions and Stellar Type Limits

We detect radio continuum sources toward four of the clumps. Two of these are unresolved, optically thick

TABLE 5  
CLUMP ACTIVITY

Clump	3.6 cm Flux <sup>a</sup> (mJy)	H II Region Type	“Green Fuzzy” <sup>?b</sup> Y/N	24 $\mu$ m flux <sup>b</sup> (mJy)	H <sub>2</sub> O maser <sup>?b</sup> (Y/N)	CH <sub>3</sub> OH maser <sup>?b</sup> (Y/N)	Clump <sup>c</sup> Activity	Evolutionary <sup>d</sup> Stage
G022.35+00.41								
GLM1	0.06	–	Y	13	Y	Y	A	2
GLM2	0.36	–	N	–	N	N	Q	1
G023.60+00.00								
GLM1(VLA4)	0.30	UCH II	Y	1058	Y	N	A	3
GLM2	0.12	–	N	198	Y	N	I	2
G024.33+00.11								
GLM1(VLA2)	0.29	UCH II	N	999	Y	Y	A	3
GLM2	0.33	–	N	–	N	N	Q	1
G024.60+00.08								
GLM1	0.09	–	N	13	Y	N	I	2
GLM2	0.09	–	Y	342	N	N	I	2
G028.23-00.19								
GLM1	0.03	–	N	–	N	N	Q	1
G028.37+00.07								
GLM1	0.18	–	N	–	N	N	Q	1
GLM2	0.12	–	Y	45	Y	N	A	2
GLM3	0.15	–	Y	4	Y	N	A	2
GLM4 <sup>e</sup>	0.12	–	Y	22	Y	Y	A	2
G028.53-00.25								
GLM1	0.06	–	Y	16	N	N	I	2
G034.43+00.24								
GLM1(VLA3)	0.31	UCH II <sup>f</sup>	Y	1718	Y	Y	A	3
GLM2(VLA1)	10.07	UCH II	N	1401	Y	Y	A	4
GLM3	0.09	–	Y	–	Y	Y	A	2

<sup>a</sup> For point sources this is the peak flux, for the extended source, G034.43+00.24: GLM2, the flux is the integrated flux, and for no detection (as marked by a – in the 3rd column) it is the  $3\sigma$  upper limit.

<sup>b</sup> Chambers et al. (2009)

<sup>c</sup> A=Active, I=Intermediate, Q=Quiescent

<sup>d</sup> See §5 for details.

<sup>e</sup> G028.37+00.07: GLM4 slightly overlaps with the resolved H II region, G028.37+00.07 VLA1, see Table 6

<sup>f</sup> G034.43+00.24: GLM1 is a marginal detection. It may or may not be an UCH II region. See §4.5 for details.

TABLE 6  
RADIO CONTINUUM SOURCES

VLA Source	R.A. (J2000)	DECL. (J2000)	Peak 3.6 cm Flux (mJy/beam)	Total 3.6 cm Flux (mJy)	$\sigma$ (mJy/beam)	Point Source <sup>a</sup> (Y/N)
G022.35+00.41						
G023.60+00.00						
VLA1	18:34:33.1	-08:15:26.8	24.3	28.4	0.3	Y
VLA2	18:34:09.6	-08:17:49.4	1.5	68.9	0.1	N
VLA3	18:34:12.4	-08:19:01.5	1.1	1.3	0.1	Y
VLA4 (GLM1)	18:34:21.1	-08:18:12.4	0.3	0.3	0.1	Y
G024.33+00.11						
VLA1	18:35:24.0	-07:37:37.9	2.8	3.6	0.5	Y
VLA2 (GLM1)	18:35:08.1	-07:35:04.0	0.29	0.4	0.02	Y
G024.60+00.08						
G028.23-00.19						
VLA1	18:43:33.7	-04:11:48.2	0.24	0.4	0.03	Y
G028.37+00.07						
VLA1	18:42:52.9	-04:00:09.2	3.0	49.9	0.5	N
VLA2	18:42:41.4	-04:02:16.9	1.7	9.6	0.4	N
VLA3	18:43:03.5	-04:00:13.2	1.98	2.2	0.08	Y
VLA4	18:42:37.1	-04:02:02.3	1.5	1.7	0.2	Y
VLA5	18:43:04.5	-04:00:15.0	1.16	1.5	0.08	Y
VLA6	18:42:52.4	-03:59:07.0	0.38	0.4	0.04	Y
G028.53-00.25						
G034.43+00.24						
VLA1 (GLM2)	18:53:18.7	+01:24:47.2	8.79	10.1	0.07	N
VLA2	18:53:08.4	+01:29:33.9	1.00	1.1	0.08	Y
VLA3 (GLM1)	18:53:18.1	+01:25:25.4	0.31	0.4	0.06	Y

<sup>a</sup> Extended sources are plotted in Figures 13-26.

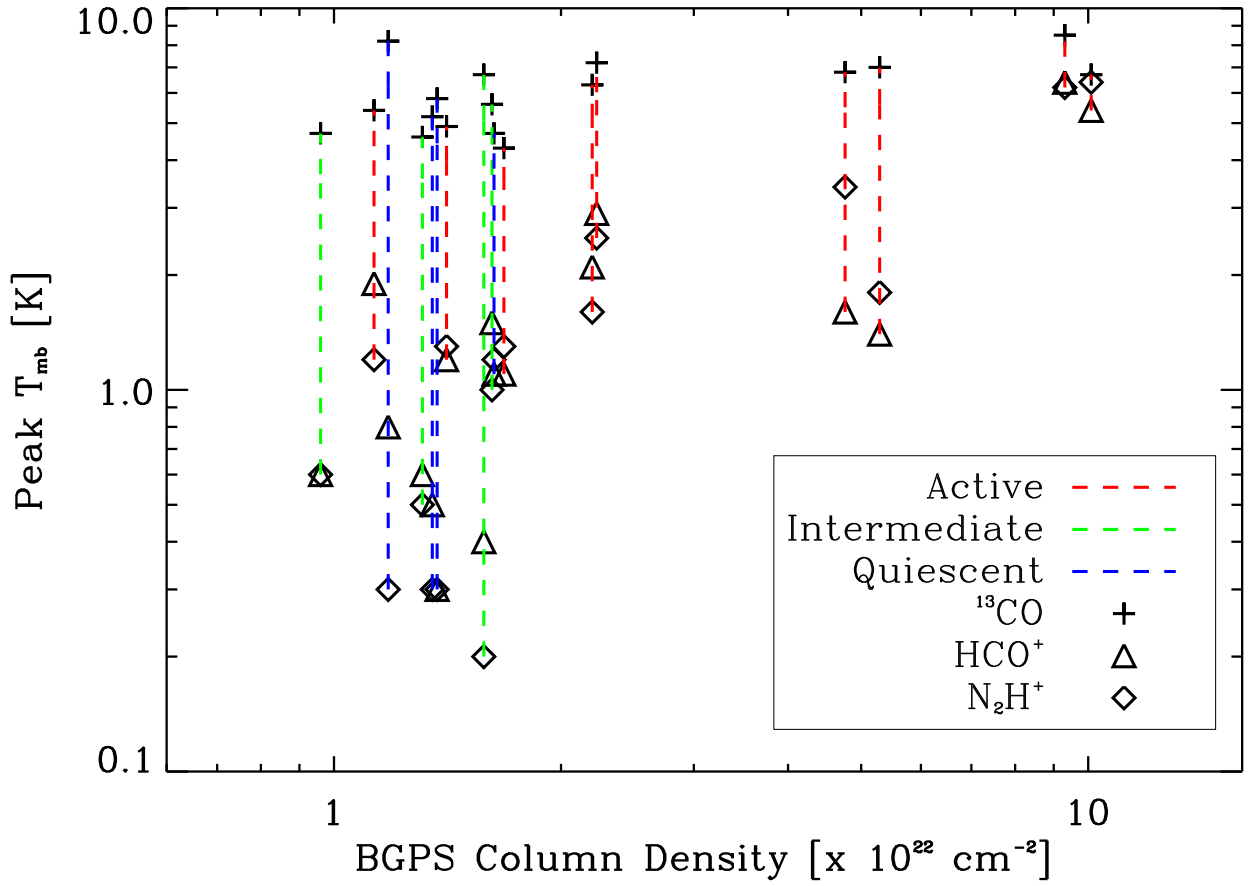


FIG. 6.— A comparison of the peak main beam temperatures for  $^{13}\text{CO}$  (cross),  $\text{HCO}^+$  (triangle), and  $\text{N}_2\text{H}^+$  (diamond) vs. BGPS column density. Each dashed line represents a single clump, and the color of the line denotes whether it is active (red), intermediate (green), or quiescent (blue). Note that  $^{13}\text{CO}$  is relatively flat with increasing column density, corroborating that it is optically thick. The variation in line strength between the various tracers (the length of the dashed line drawn) is much smaller for active vs. quiescent clumps and is a potentially useful diagnostic for understanding star formation activity.

UCH II regions. One is a slightly resolved, optically thin UCH II region. The final source is an unresolved, marginal detection which may be an UCH II region. The peak fluxes of these regions are given in Table 5, as well as the limiting ( $3\sigma$ ) flux in the clumps without detections. The properties of all the detections (outside or inside the clumps) are reported in Table 6. The sources are named based on the IRDC in which they were found (though they are not necessarily associated with the cloud) and in order of decreasing brightness (VLA1, VLA2, etc.). All the Gaussian-type sources were fit with 2-D elliptical Gaussians, and the fluxes reported are from the fits. The  $\sigma$  reported is the r.m.s. of the fit residuals. For the sources with non-Gaussian morphology, the fluxes were measured using a circular aperture and an outer annulus of equal area. The mean of the flux in the outer annulus is assumed to be the background level and is subtracted from the source flux, while the standard deviation in the outer annulus is our quoted  $\sigma$ . Some of these detections are more evolved H II regions, peripheral to the IRDC. Others are point sources unassociated with any GLIMPSE emission. These sources may be unresolved H II regions that happen to be in our field of view but unassociated with the mid-IR, or they may be other types of Galactic or extragalactic radio continuum sources. We restrict our analysis to the four radio continuum sources associated with the millimeter clump peaks, as these are almost certainly UCH II regions in the IRDC.

The UCH II region radio continuum flux is directly related to the number of Lyman continuum photons ( $Q$ ) of the ionizing star if the region is optically thin. Through comparison with the 20 cm and 6 cm radio continuum data from the Multi-Array Galactic Plane Imaging Survey (MAGPIS; White et al. 2005) we find that G034.43+00.24: GLM2 (VLA1) is slightly resolved ( $D \sim 0.14$  pc) and optically thin at 3.6 cm. G034.43+00.24: GLM1 (VLA3) is a marginal detection in both our survey and the 6 cm survey by Shepherd et al. (2004). The measured flux densities at 3.6 and 6 cm are not consistent with the source being an UCH II region. However, the fluxes reported are highly uncertain, and systematic errors could be large enough to account for this inconsistency if it is in fact an UCH II region. Since an optically thick UCH II region is the most likely explanation for a radio continuum source associated with star formation in an IRDC clump, we assume that this is the explanation for the radio continuum source. We use the 3.6 cm flux to calculate the Lyman continuum flux of an unresolved, optically thick, UCH II region, but acknowledge that this assumption may be incorrect. For G024.33+00.11: GLM1 (VLA2) and G023.60+00.00: GLM1 (VLA4) the 6 cm upper limits are consistent with the source being an optically thick UCH II region at 3.6 cm.

In the optically thin case (G034.43+00.24: GLM2 (VLA1)), we fit a thermal bremsstrahlung curve to the 3.6, 6, and 20 cm points. We find an emission measure  $EM = 4.4 \times 10^6 \text{ cm}^{-6} \text{ pc}$ , a turnover frequency  $\nu(\tau = 1) = 1.3 \text{ GHz}$ , and  $Q = 6.1 \times 10^{45}$  Lyman continuum photons per second. This translates to a B0.5 star (Vacca et al. 1996), in agreement with Shepherd et al. (2004).

For the unresolved, optically thick sources, we first de-

rive a source radius

$$r = \left[ \frac{S_\nu c^2}{2\nu^2 k T_e} 4D^2 \right]^{1/2} \quad (20)$$

where  $S_\nu$  is the radio continuum flux,  $\nu$  is the band-center frequency,  $T_e$  is the ionized gas temperature, and  $D$  is the distance. We assume a  $T_e = 8000 \text{ K}$  ionized gas, typical of an H II region. We conservatively assume that the observed frequency is the turnover frequency (where  $\tau = 1$ ). This gives us a lower limit for the emission measure (EM), electron density ( $n_e$ ), and number of Lyman continuum photons ( $Q$ ). If our observing frequency is the turnover frequency ( $\nu$ ) then  $\tau = 1$  in our expression for the emission measure (Wood & Churchwell 1989)

$$EM(\text{cm}^{-6} \text{ pc}) = \frac{\tau}{8.235 \times 10^{-2} \alpha(\nu, T_e) T_e^{-1.35} \nu^{-2.1}}. \quad (21)$$

The lower limit for the number density of electrons, which we take to be equal the number density of ions, is

$$n_e = \sqrt{\frac{EM}{2r}}. \quad (22)$$

The number of Lyman continuum photons is given by the Stromgren sphere equation,

$$Q = \frac{4}{3} \pi r^3 \alpha_B n_e^2 \quad (23)$$

where  $\alpha_B$  is the recombination rate coefficient,  $3.1 \times 10^{-13} \text{ cm}^3 \text{ s}^{-1}$  for  $T_e = 8000 \text{ K}$ . The Stromgren sphere equation assumes that the H II region is spherical, in equilibrium, that there is one electron per ion, and that each energetic photon ionizes an atom or molecule. Since the observed structure is clumpy, the Stromgren sphere approximation is probably not a very good one. Using this method for the two (possibly three) optically thick, unresolved UCH II regions yields a  $\log(Q)$  of 46.14, 46.55, and 46.15 and stellar types (Vacca et al. 1996) of B0, O9.5, and B0 for G023.60+00.00: GLM1 (VLA4), G024.33+00.11: GLM1 (VLA2), and G034.43+00.24: GLM1 (VLA3) respectively.

#### 4.6. Clump Activity

A major driving question in the study of IRDCs is the evolutionary sequence of the clumps and clouds: identifying the different evolutionary stages and their relative lifetimes. This requires an understanding of the star formation activity. We employ four different star formation tracers: 1) an embedded  $24 \mu\text{m}$  point source, 2) “green fuzzies,” regions of enhanced, extended  $4.5 \mu\text{m}$  emission, indicative of shocks and outflows, 3)  $\text{H}_2\text{O}$  and Class I  $\text{CH}_3\text{OH}$  maser emission, and finally, 4) Ultra-Compact (UC) H II regions, an unambiguous indication that a massive star that has “turned on.” Tracers of star formation activity in these clumps are summarized in Table 5.

Each of these tracers is sensitive to somewhat different environments. A  $24 \mu\text{m}$  point source traces material accreting onto forming stars, the gravitational contraction of a young stellar object (YSO), or even the nuclear energy emitted once the star has “turned on.” “Green



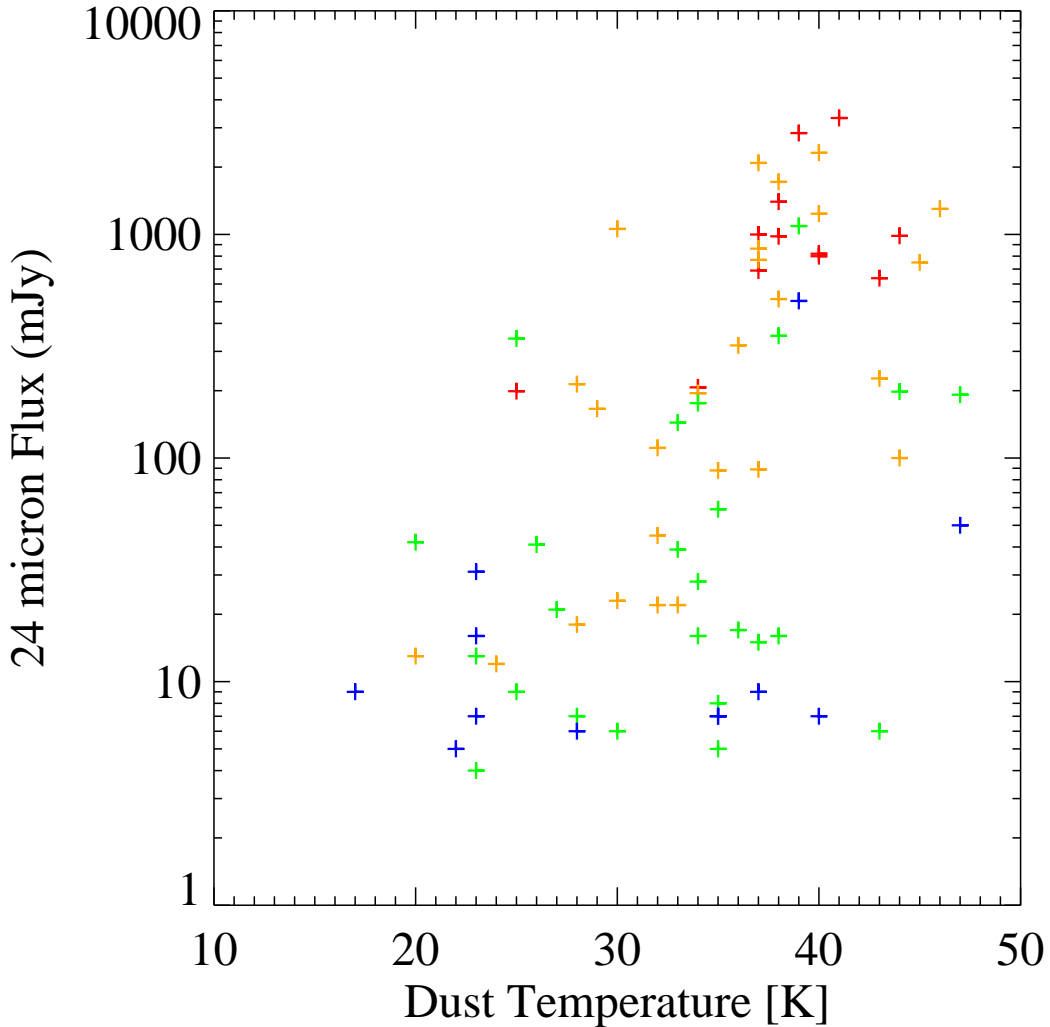


FIG. 7.— 24  $\mu\text{m}$  flux (as measured by Chambers et al. 2009) vs. dust temperature (from Rathborne et al. 2010) for the red: “red” clumps, orange: clumps with three star formation tracers, green: two star formation tracers, and blue: one star formation tracer. Note that the “red” clumps are associated with brighter 24  $\mu\text{m}$  flux and that in general, the more tracers of star formation activity, the warmer the clump.

fuzzies” (Chambers et al. 2009; Cyganowski et al. 2008, also called Extended Green Objects, EGOs) are thought to arise from shock-excited spectral line emission (Marston et al. 2004; Noriega-Crespo et al. 2004) due to outflows from young stars. Many of the  $\text{HCO}^+$  and  $\text{N}_2\text{H}^+$  spectra (see Figures 11(b) to 26(d)) show asymmetric line profiles commonly associated with outflows, many of which (e.g. G034.43+00.24 GLM3, Figure 26(d)) are associated with “green fuzzies,” further implicating “green fuzzies” as positive outflow tracers.  $\text{H}_2\text{O}$  (22.23 GHz) and  $\text{CH}_3\text{OH}$  (Class I 24.96 GHz) masers are well-known signposts of star formation activity, likely formed in shocks and outflows. Finally, we include the presence of 3.6 cm radio continuum emission which when associated with a millimeter peak or mid-IR emission is a clear indicator of an UCH II region.

Together, these tracers are sensitive to warm, embedded dust indicative of accretion, shocks and outflows, and thermal bremsstrahlung from newly formed H II re-

gions. While these are all excellent tracers of star formation, none are perfect, so we would not expect to see every tracer in every actively star-forming region. Viewing angle or dust obscuration could play a significant role in a non-detection. We assign the designation “active” to clumps that exhibit three or four signs of active star formation (“green fuzzy,” 24  $\mu\text{m}$  point source, UCH II region, or maser emission). This ensures that each “active” clump has either an H II region (unambiguously star-forming) or at least two outflow tracers (maser emission or “green fuzzy”) and a 24  $\mu\text{m}$  point source. We assign the designation “quiescent” to clumps that exhibit no signs of active star formation. We reserve the title “intermediate” for clumps which exhibit one or two signs of active star formation. Intermediate clumps, therefore, may have only shock/outflow signatures or a 24  $\mu\text{m}$  point source. These categorizations represent a crude separation between the quiet, massive-starless clumps and the active, star-forming clumps, not

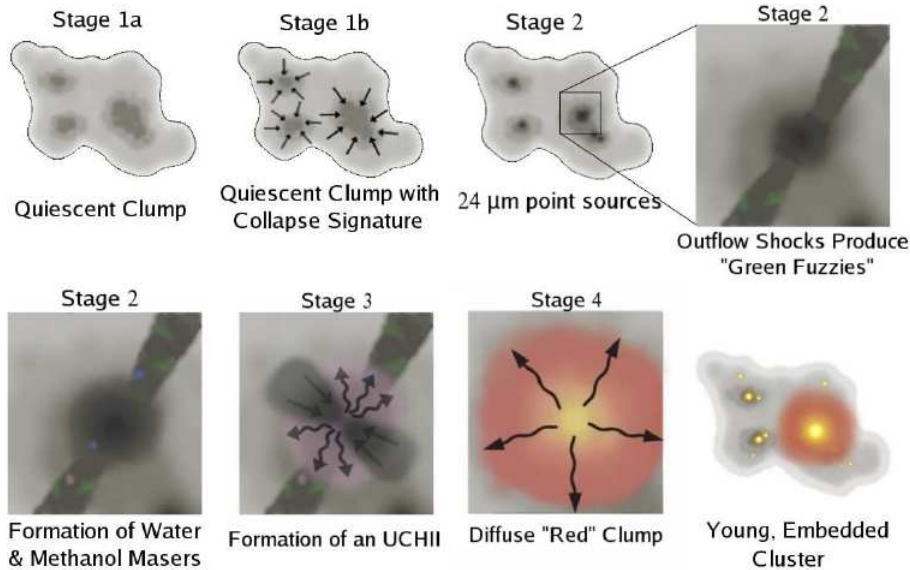


FIG. 8.— A cartoon depiction of the discussed evolutionary sequence. See §5 for details.

an evolutionary sequence. Evolutionary sequences are discussed in §5.

The detection of several UCH II regions embedded in IRDC clumps unambiguously shows that some IRDCs are forming massive stars. We note that all the clumps associated with UCH II regions have significantly brighter ( $\gtrsim 1$  Jy)  $24 \mu\text{m}$  flux. All but one of the UCH II regions are associated with a  $\text{CH}_3\text{OH}$  maser and two of the four have a “green fuzzy.” The lack of “green fuzzies” and a  $\text{CH}_3\text{OH}$  maser in some sources may indicate that the outflow stage has ceased, or could simply be related to an unfavorable viewing angle. We also note that the brightest UCH II regions (G034.43+00.24: GLM2 and near the edge of G028.37+00.07: GLM4) are associated with “diffuse red clumps,” regions of extended, enhanced  $8 \mu\text{m}$  emission. The ionizing radiation from a young H II region will excite PAH features in the  $8 \mu\text{m}$  band. As the H II region grows it will begin to clear some of the surrounding dust and gas and reveal itself as a “diffuse red clump.” As the H II region continues to evolve, there will be PAH destruction by the strong UV flux and it will no longer have enhanced  $8 \mu\text{m}$  emission. The clumps which contain UCH II regions, but are not classified as “red” are either in an earlier evolutionary phase or are perhaps still obscured by the dust at  $8 \mu\text{m}$ . There are no “diffuse red clumps” in our sample which are not associated with UCH II regions, so these are potentially very useful tracers of young H II regions.

Chambers et al. (2009) discussed the use of “red clumps” (regions of enhanced  $8 \mu\text{m}$  emission) as tracers of embedded H II regions. Since an enhancement at  $8 \mu\text{m}$  could presumably be caused by any significant UV flux and most high column density clumps are nearly optically thick at  $8 \mu\text{m}$ , we suggest that only the more diffuse “red clumps” are necessarily associated with H II regions. Only when the forming star has cleared out some dust obscuration and is no longer associated with a millimeter *peak* can it be identified as a “diffuse red clump.” Other “red clumps” could be embedded UCH II regions that have not cleared out their envelopes, or they could

be PAH nebulae excited by main sequence or evolved AB stars.

Figure 7 shows the  $24 \mu\text{m}$  flux (as measured by Chambers et al. 2009) vs. the dust temperature (measured through SED fits in the sample of 100 clumps by Rathborne et al. 2010). Notice that the “red” clumps are associated with brighter  $24 \mu\text{m}$  flux and that in general, the more star formation tracers, the warmer the clump is. This general trend indicates that these tracers combined are successfully measuring star formation activity. However, the large scatter may be due to viewing angle biases, mis-assigned star formation tracers, or the inadequacy of single-temperature SED fits.

## 5. DISCUSSION OF AN EVOLUTIONARY SEQUENCE FOR IRDC CLUMPS

Based on a sample of 190 IRDC clumps, Chambers et al. (2009) proposed an evolutionary sequence for IRDC clumps which begins with a quiescent clump (in their definition, this means no “green fuzzy” or  $24 \mu\text{m}$  point source), transitions into an active clump (the clump contains a “green fuzzy” and a  $24 \mu\text{m}$  point source), and finally, becomes a “red” (enhanced  $8 \mu\text{m}$  emission) clump. Our radio continuum data support this sequence, especially that the final evolutionary stage is a “red” clump, in which the H II region is exciting the PAH spectral feature in the  $8 \mu\text{m}$  band. However, we suggest that the term “red” clump be reserved for more diffuse, evolved “red” clumps, not associated with a millimeter peak. This prevents any confusion with embedded B or A stars which have UV luminosity significant enough to excite the PAH emission in the  $8 \mu\text{m}$  band, but not enough to produce an UCH II region. Some clumps with H II regions are “red” and some are not, which may indicate different environments or evolutionary stages. Clumps with UCH II regions tend to have a significantly brighter  $24 \mu\text{m}$  source flux ( $\gtrsim 1$  Jy).

Presented in Figure 8 is a cartoon of star formation tracers and how they may possibly relate to evolution-

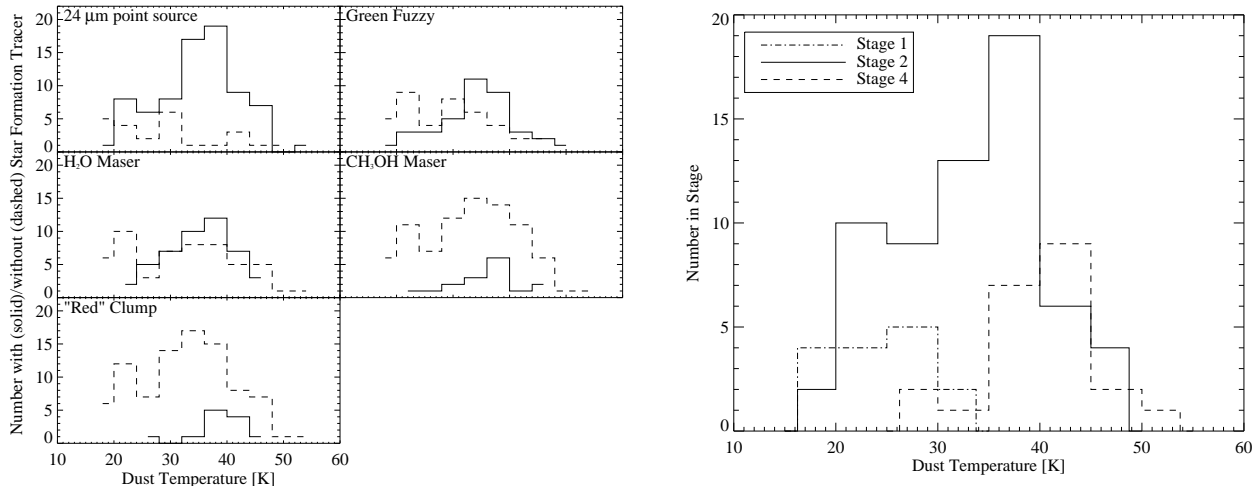


FIG. 9.— Left: For each star formation activity tracer used, we plot a dust temperature (as measured by Rathborne et al. 2010) histogram of the clumps with (solid line) and without (dashed line) that star formation tracer (as measured by Chambers et al. 2009) from the sample of Rathborne et al. (2010). Note that all the star formation tracers exist over a wide range of temperatures, except for “red” clumps which are found primarily at higher temperatures. The top four panels are Stage 2 sources while the “red” clump panel are Stage 4 sources (see Section 5). Right: A dust temperature histogram of possible evolutionary stages in the sample of 100 clumps from Rathborne et al. (2010). This sample is likely incomplete at the low-temperature end, as many of the coldest sources would also be faint and below the detection threshold for the SED fits.

ary stages. Stage 1 is a quiescent clump; a cold, millimeter peak with no signs of active star formation. Stage 1 can be split into two sub-categories: a) a quiescent clump which has not yet begun to collapse and b) a quiescent clump that shows collapse signatures, but no signs of active star formation. The next stage is a hotter, denser clump that shows signs of active star formation. Stage 2 is a clump with at least 1 sign of active star formation, a 24  $\mu\text{m}$  point source, “green fuzzy,” or a H<sub>2</sub>O or CH<sub>3</sub>OH maser. We cannot infer any sequential nature between these observational signatures at this time. However, the authors hypothesize that, in analogy with low-mass star forming regions, an outflow (“green fuzzy”) and 24  $\mu\text{m}$  point source will occur first (the one seen first depends on viewing angle), followed by an H<sub>2</sub>O maser, and then a CH<sub>3</sub>OH maser as the accreting protostars gain mass.

The third stage in this sequence is the ignition of an UCH II region (see Figure 8). A Stage 3 source will have a strong ( $\gtrsim 1$  Jy) 24  $\mu\text{m}$  point source and possibly maser emission and outflow indicators. Modern theory (e.g. McKee & Ostriker 2007) suggests that massive stars reach the main sequence while still accreting, because the accretion time scale is greater than the Kelvin-Helmholtz timescale. Thus, a main-sequence B star may continue to accrete on the main sequence, eventually becoming an O star. A Stage 3 source, therefore, may remain compact and continue accreting for some time. The fourth stage in this evolutionary sequence is the expansion of the H II region, producing a diffuse “red” clump (see Figure 8). However, this is not a necessary condition for massive star formation, as in the densest cores, the H II region may be quenched by the remaining envelope (Keto 2003) for some time and a “diffuse red clump” will not form. For UCH II regions not trapped by their surrounding envelope, the UCH II region will expand as the radiation field increases or instabilities develop. This expansion evacuates a dust cavity, creating a diffuse enhancement at 8  $\mu\text{m}$ , that is spatially distinct from any millimeter

continuum peaks. In Table 5 we assign each clump to these coarse evolutionary stages.

One potential test of the sequential nature of star formation tracers is the clump temperature. We suggest that as a clump evolves, its temperature monotonically increases with time. In a statistical sense, warmer objects should be more evolved than colder objects. We use the dust temperatures derived by Rathborne et al. (2010) in a sample of 100 clumps and the star formation tracers as catalogued by Chambers et al. (2009) to investigate how dust temperatures change with star formation tracers in Figure 9. All of the individual star formation tracers exist over a surprisingly wide range of temperatures, except for “red” clumps which are found primarily at higher temperatures. Figure 7 shows that the more star formation tracers a clump has, the warmer it is on average, however, no sequential nature can be inferred between the individual star formation tracers in Stage 2. The lower panel of Figure 9 shows that the broad categorizations between Stage 1 (quiescent), Stage 2 (intermediate/active), and Stage 4 (“diffuse red clump”) clumps are well-separated by temperature, and likely represent a true evolutionary sequence (we note that many Stage 1 clumps were too faint to reliably fit an SED, so the true histogram is likely even further to the colder side of the histogram). These data support the coarse separation of Stage 1, Stage 2, and Stage 4 clumps as an evolutionary sequence, however, no further sequential nature of star formation tracers can be inferred.

When discussing evolutionary sequences, there is always the added uncertainty of whether we are truly seeing an evolutionary sequence or just different environments. We point out that it is likely that not all Stage 1 (quiescent) clumps will form Stage 2 (active) clumps, however, we are suggesting that all Stage 2 clumps form from Stage 1 clumps and so on. Some quiescent clumps may be forming low/intermediate mass stars which will remain undetected by our star formation tracers. Alternatively, some quiescent clumps may be transient density

enhancements which will eventually disperse. This makes the question of lifetimes more complicated. The lack of a sequence between the observed star formation tracers is a bit surprising, however, the fact that more star formation tracers indicates a higher temperature indicates that viewing angle/obscuration may be playing a large role in the observed scatter. Perhaps only when a clump is more evolved and somewhat less obscured by dust can one detect many of these star formation tracers. Higher sensitivity and better spatial resolution observations, as well as a better control of systematics may reveal some sequential nature between the observed star formation tracers. We note that the overlap of the Stage 2 and Stage 4 sources in Figure 9(b) hint at some number of UCH II regions undetected as “red” clumps or some number of “red” clumps incorrectly associated with UCH II regions.

## 6. CONCLUSION

We examined a sample of 17 clumps within 8 IRDCs using existing infrared, millimeter, and radio data, as well as new VLA radio continuum and HHT dense gas spectral data. Our main conclusions are:

- 8  $\mu\text{m}$  extinction mass and BGPS 1.1 mm mass are complementary tracers of mass in IRDCs, except for the most active clumps (notably those containing UCH II regions), for which both mass tracers suffer biases.
- The measured virial masses of IRDC clumps are uniformly larger than the dust continuum masses on the scale of  $\sim 1$  pc.
- We do not detect a chemical differentiation of  $\text{HCO}^+$  and  $\text{N}_2\text{H}^+$  between active and quiescent clumps on the scale of  $\sim 1$  pc. However, both  $\text{HCO}^+$  and  $\text{N}_2\text{H}^+$  are brighter in active clumps, due to an increase in temperature and/or density.
- We report the identification of four UCH II regions embedded within IRDC clumps. We find that UCH II regions are associated with bright ( $\gtrsim 1$  Jy)

24  $\mu\text{m}$  point sources, and the brightest UCH II regions are associated with “diffuse red clumps” (an extended enhancement at 8  $\mu\text{m}$ ).

- We discuss an evolutionary sequence for cluster-forming clumps and find that the sequential separation of the broad evolutionary stages, quiescent, active, and “diffuse red clumps,” is supported by dust temperatures, however, no sequential nature can be inferred between the individual star formation tracers.

We are thankful to our referee, Sean Carey, for a thorough and insightful review, which has significantly improved the quality of this manuscript. We are grateful to Edward Chambers, Jeremy Darling, Erica Ellingson, Susanna Finn, Michael Shull, and Irena Stojimirović for useful comments and discussion. This work has made use of the GLIMPSE and MIPS GAL surveys, and we thank those teams for their help and support. We would like to thank the staff at the HHT and VLA for their assistance. The National Radio Astronomy Observatory is a facility of the National Science Foundation operated under cooperative agreement by Associated Universities, Inc. The BGPS project is supported by the National Science Foundation through NSF grant AST-0708403. We are grateful to Jill Rathborne for sharing her MAMBO 1.2 mm data. This publication makes use of molecular line data from the Boston University-FCRAO Galactic Ring Survey (GRS). The GRS is a joint project of Boston University and Five College Radio Astronomy Observatory, funded by the National Science Foundation under grants AST-9800334, AST-0098562, AST-0100793, AST-0228993, & AST-0507657. This work has made use of ds9, APLPY (aplypy.sourceforge.net), and the Goddard Space Flight Center’s IDL Astronomy Library. C.B. is supported by the National Science Foundation (NSF) through the Graduate Research Fellowship Program (GRFP).

*Facilities:* HHT, VLA, Spitzer (IRAC), Spitzer (MIPS), CSO (Bolocam)

## REFERENCES

- Aguirre, J. A., Ginsburg, A. G., Dunham, M. K., Drosback, M. D., Bally, J., Battersby, C., Bradley, E., Cyganowski, C., Dowell, D., Evans II, N. J., Glenn, J., Harvey, P. M., Rosolowsky, E. W., Stringfellow, G., Walawender, J., & Williams, J. P. 2010, submitted
- Benjamin, R. A., Churchwell, E., Babler, B. L., Bania, T. M., Clemens, D. P., Cohen, M., Dickey, J. M., Indebetouw, R., Jackson, J. M., Kobulnicky, H. A., Lazarian, A., Marston, A. P., Mathis, J. S., Meade, M. R., Seager, S., Stolovy, S. R., Watson, C., Whitney, B. A., Wolff, M. J., & Wolfire, M. G. 2003, *PASP*, 115, 953
- Beuther, H., Sridharan, T. K., & Saito, M. 2005, *ApJ*, 634, L185
- Butler, M. J., & Tan, J. C. 2009, *ApJ*, 696, 484
- Carey, S. J., Clark, F. O., Egan, M. P., Price, S. D., Shipman, R. F., & Kuchar, T. A. 1998, *ApJ*, 508, 721
- Carey, S. J., Feldman, P. A., Redman, R. O., Egan, M. P., MacLeod, J. M., & Price, S. D. 2000, *ApJ*, 543, L157
- Carey, S. J., Noriega-Crespo, A., Mizuno, D. R., Shenoy, S., Paladini, R., Kraemer, K. E., Price, S. D., Flagey, N., Ryan, E., Ingalls, J. G., Kuchar, T. A., Pinheiro Gonçalves, D., Indebetouw, R., Billot, N., Marleau, F. R., Padgett, D. L., Rebull, L. M., Bressert, E., Ali, B., Molinari, S., Martin, P. G., Berriman, G. B., Boulanger, F., Latter, W. B., Miville-Deschenes, M. A., Shipman, R., & Testi, L. 2009, *PASP*, 121, 76
- Chambers, E. T., Jackson, J. M., Rathborne, J. M., & Simon, R. 2009, *ApJS*, 181, 360
- Cyganowski, C. J., Whitney, B. A., Holden, E., Braden, E., Brogan, C. L., Churchwell, E., Indebetouw, R., Watson, D. F., Babler, B. L., Benjamin, R., Gomez, M., Meade, M. R., Povich, M. S., Robitaille, T. P., & Watson, C. 2008, *AJ*, 136, 2391
- Daniel, F., Cernicharo, J., Roueff, E., Gerin, M., & Dubernet, M. L. 2007, *ApJ*, 667, 980
- de Wit, W. J., Testi, L., Palla, F., & Zinnecker, H. 2005, *A&A*, 437, 247
- Du, F., & Yang, J. 2008, *ApJ*, 686, 384

- Dunham, M. K., Rosolowsky, E., Evans II, N. J., C. C., Aguirre, J. A., Bally, J., Battersby, C., Bradley, E., Dowell, D., Drosback, M. D., Ginsburg, A. G., Glenn, J., Harvey, P. M., Merello, M., Schlingman, W., Shirley, Y. L., Stringfellow, G., Walawender, J., & Williams, J. P. 2010, submitted
- Egan, M. P., Shipman, R. F., Price, S. D., Carey, S. J., Clark, F. O., & Cohen, M. 1998, *ApJ*, 494, L199+
- Enoch, M. L., Young, K. E., Glenn, J., Evans, II, N. J., Golwala, S., Sargent, A. I., Harvey, P., Aguirre, J., Goldin, A., Haig, D., Huard, T. L., Lange, A., Laurent, G., Maloney, P., Maukopf, P., Rossinot, P., & Sayers, J. 2006, *ApJ*, 638, 293
- Glenn, J., Ade, P. A. R., Amarie, M., Bock, J. J., Edgington, S. F., Goldin, A., Golwala, S., Haig, D., Lange, A. E., Laurent, G., Maukopf, P. D., Yun, M., & Nguyen, H. 2003, in *Society of Photo-Optical Instrumentation Engineers (SPIE) Conference Series*, Vol. 4855, *Society of Photo-Optical Instrumentation Engineers (SPIE) Conference Series*, ed. T. G. Phillips & J. Zmuidzinas, 30–40
- Heitsch, F., Hartmann, L. W., Slyz, A. D., Devriendt, J. E. G., & Burkert, A. 2008, *ApJ*, 674, 316
- Jackson, J. M., Rathborne, J. M., Shah, R. Y., Simon, R., Bania, T. M., Clemens, D. P., Chambers, E. T., Johnson, A. M., Dormody, M., Lavoie, R., & Heyer, M. H. 2006, *ApJS*, 163, 145
- Jørgensen, J. K., Schöier, F. L., & van Dishoeck, E. F. 2004, *A&A*, 416, 603
- Kauffmann, J., Bertoldi, F., Bourke, T. L., Evans, II, N. J., & Lee, C. W. 2008, *A&A*, 487, 993
- Keto, E. 2003, *ApJ*, 599, 1196
- Lada, C. J., & Lada, E. A. 2003, *ARA&A*, 41, 57
- Lucas, R., & Liszt, H. 1998, *A&A*, 337, 246
- Mangum, J. G., Emerson, D. T., & Greisen, E. W. 2007, *A&A*, 474, 679
- Marston, A. P., Reach, W. T., Noriega-Crespo, A., Rho, J., Smith, H. A., Melnick, G., Fazio, G., Rieke, G., Carey, S., Rebull, L., Muzerolle, J., Egami, E., Watson, D. M., Pipher, J. L., Latter, W. B., & Stapelfeldt, K. 2004, *ApJS*, 154, 333
- McKee, C. F., & Ostriker, E. C. 2007, *ARA&A*, 45, 565
- McKee, C. F., & Tan, J. C. 2003, *ApJ*, 585, 850
- McKee, C. F., & Williams, J. P. 1997, *ApJ*, 476, 144
- Mueller, K. E., Shirley, Y. L., Evans, II, N. J., & Jacobson, H. R. 2002, *ApJS*, 143, 469
- Noriega-Crespo, A., Morris, P., Marleau, F. R., Carey, S., Boogert, A., van Dishoeck, E., Evans, II, N. J., Keene, J., Muzerolle, J., Stapelfeldt, K., Pontoppidan, K., Lowrance, P., Allen, L., & Bourke, T. L. 2004, *ApJS*, 154, 352
- Omont, A., Gilmore, G. F., Alard, C., Aracil, B., August, T., Baliyan, K., Beaulieu, S., Bégon, S., Bertou, X., Blommaert, J. A. D. L., Borsenberger, J., Burgdorf, M., Caillaud, B., Cesarsky, C., Chitre, A., Copet, E., de Batz, B., Egan, M. P., Egret, D., Epchtein, N., Felli, M., Fouqué, P., Ganesh, S., Genzel, R., Glass, I. S., Gredel, R., Groenewegen, M. A. T., Guglielmo, F., Habing, H. J., Hennebelle, P., Jiang, B., Joshi, U. C., Kimeswenger, S., Messineo, M., Miville-Deschênes, M. A., Moneti, A., Morris, M., Ojha, D. K., Ortiz, R., Ott, S., Parthasarathy, M., Péroult, M., Price, S. D., Robin, A. C., Schultheis, M., Schuller, F., Simon, G., Soive, A., Testi, L., Teyssier, D., Tiphène, D., Unavane, M., van Loon, J. T., & Wyse, R. 2003, *A&A*, 403, 975
- Ossenkopf, V., & Henning, T. 1994, *A&A*, 291, 943
- Péroult, M., Omont, A., Simon, G., Seguin, P., Ojha, D., Blommaert, J., Felli, M., Gilmore, G., Guglielmo, F., Habing, H., Price, S., Robin, A., de Batz, B., Cesarsky, C., Elbaz, D., Epchtein, N., Fouque, P., Guest, S., Levine, D., Pollock, A., Prusti, T., Siebenmorgen, R., Testi, L., & Tiphène, D. 1996, *A&A*, 315, L165
- Peretto, N., & Fuller, G. A. 2009, *A&A*, 505, 405
- Ragan, S. E., Bergin, E. A., & Gutermuth, R. A. 2009, *ApJ*, 698, 324
- Rathborne, J. M., Jackson, J. M., Chambers, E. T., Stojimirovic, I., Simon, R., Shipman, R., & Frieswijk, W. 2010, *ArXiv e-prints*
- Rathborne, J. M., Jackson, J. M., & Simon, R. 2006, *ApJ*, 641, 389
- Rathborne, J. M., Jackson, J. M., Zhang, Q., & Simon, R. 2008, *ApJ*, 689, 1141
- Rathborne, J. M., Simon, R., & Jackson, J. M. 2007, *ApJ*, 662, 1082
- Reach, W. T., Rho, J., Tappe, A., Pannuti, T. G., Brogan, C. L., Churchwell, E. B., Meade, M. R., Babler, B., Indebetouw, R., & Whitney, B. A. 2006, *AJ*, 131, 1479
- Redman, R. O., Feldman, P. A., Wyrowski, F., Côté, S., Carey, S. J., & Egan, M. P. 2003, *ApJ*, 586, 1127
- Reid, M. J., & Ho, P. T. P. 1985, *ApJ*, 288, L17
- Reid, M. J., Menten, K. M., Zheng, X. W., Brunthaler, A., Moscadelli, L., Xu, Y., Zhang, B., Sato, M., Honma, M., Hirota, T., Hachisuka, K., Choi, Y. K., Moellenbrock, G. A., & Bartkiewicz, A. 2009, *ArXiv e-prints*
- Rosolowsky, E., Dunham, M. K., Ginsburg, A., Bradley, E. T., Aguirre, J., Bally, J., Battersby, C., Cyganowski, C., Dowell, D., Drosback, M., Evans, N. J., Glenn, J., Harvey, P., Stringfellow, G. S., Walawender, J., & Williams, J. P. 2010, *ApJS*, 188, 123
- Shepherd, D. S., Nürnberger, D. E. A., & Bronfman, L. 2004, *ApJ*, 602, 850
- Shirley, Y. L., Evans, II, N. J., Young, K. E., Knez, C., & Jaffe, D. T. 2003, *ApJS*, 149, 375
- Simon, R., Jackson, J. M., Rathborne, J. M., & Chambers, E. T. 2006a, *ApJ*, 639, 227
- Simon, R., Rathborne, J. M., Shah, R. Y., Jackson, J. M., & Chambers, E. T. 2006b, *ApJ*, 653, 1325
- Tafalla, M., Myers, P. C., Caselli, P., Walmsley, C. M., & Comito, C. 2002, *ApJ*, 569, 815
- Vacca, W. D., Garmany, C. D., & Shull, J. M. 1996, *ApJ*, 460, 914
- Wang, Y., Zhang, Q., Pillai, T., Wyrowski, F., & Wu, Y. 2008, *ApJ*, 672, L33
- White, R. L., Becker, R. H., & Helfand, D. J. 2005, *AJ*, 130, 586
- Wood, D. O. S., & Churchwell, E. 1989, *ApJS*, 69, 831
- Wyrowski, F., Carey, S. J., Egan, M. P., Feldman, P. A., & Redman, R. O. 2000, in *Bulletin of the American Astronomical Society*, Vol. 197, *Bulletin of the American Astronomical Society*, 515–+
- Zhang, Q., Wang, Y., Pillai, T., & Rathborne, J. 2009, *ApJ*, 696, 268
- Zinnecker, H., & Yorke, H. W. 2007, *ARA&A*, 45, 481

## APPENDIX

## INDIVIDUAL CLUMPS AND CLOUDS

This appendix explores the properties of each cloud in more detail. Presented are GLIMPSE three-color images of each cloud with MAMBO 1.2 mm contours and MIPS GAL 24  $\mu$ m images with BGPS 1.1 mm contours. For clouds

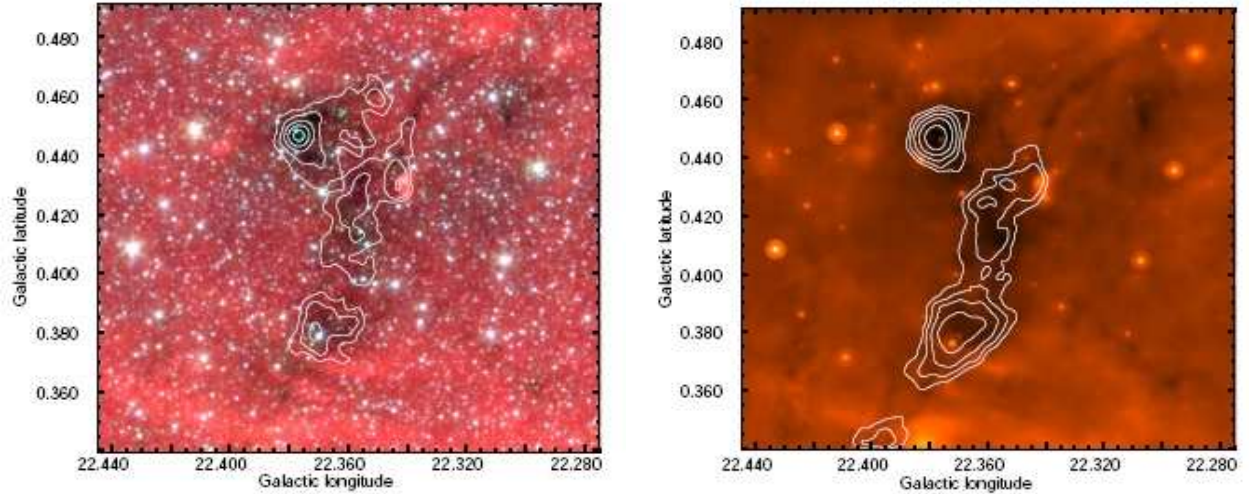


FIG. 10.— G022.35+00.41: Left: GLIMPSE three-color image, red is  $8\ \mu\text{m}$ , green is  $4.5\ \mu\text{m}$  and blue is  $3.6\ \mu\text{m}$  with MAMBO 1.2 mm contours overlaid. The contours are on a log scale from 15 to 410  $\text{mJy beam}^{-1}$ . Right: MIPS GAL  $24\ \mu\text{m}$  image with BGPS 1.1 mm contours. The contours are on a log scale from 0.12 to 0.7  $\text{Jy beam}^{-1}$ .

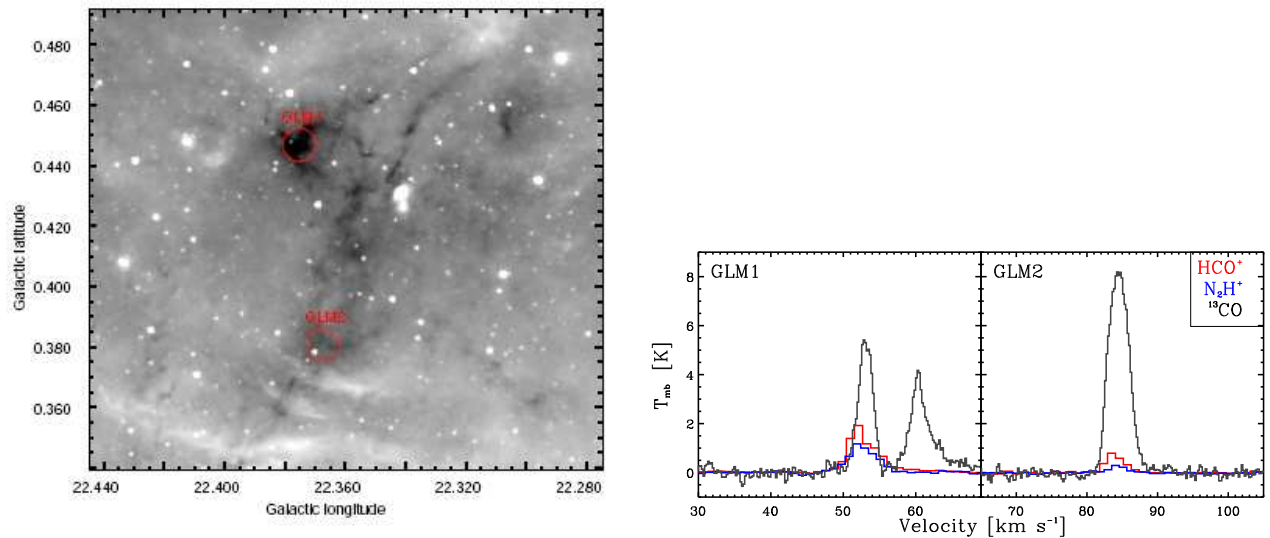


FIG. 11.— G022.35+00.41: Left: GLIMPSE  $8\ \mu\text{m}$  overlaid with the BGPS beam-sized apertures that were used to determine clump masses. Right:  $\text{HCO}^+$ ,  $\text{N}_2\text{H}^+$  and  $^{13}\text{CO}$  spectra in clumps GLM1 (Stage 2) and GLM2 (Stage 1).

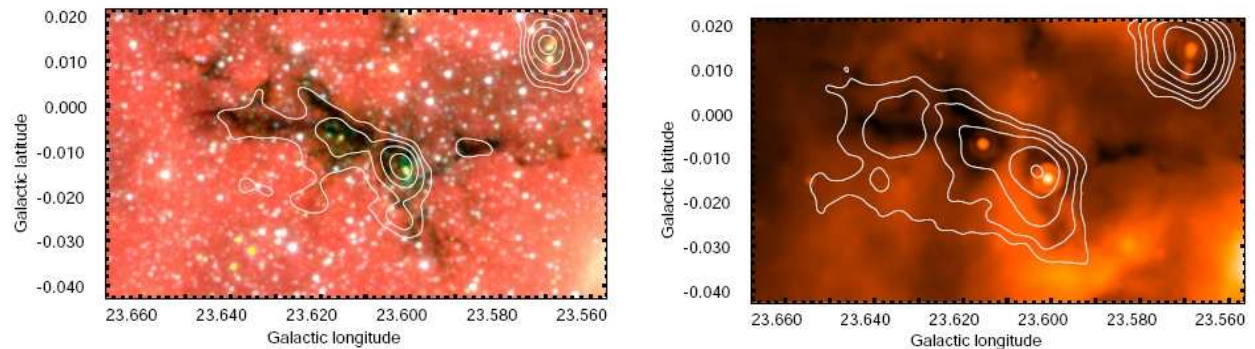


FIG. 12.— G023.60+00.00: Left: GLIMPSE three-color image, red is  $8\ \mu\text{m}$ , green is  $4.5\ \mu\text{m}$  and blue is  $3.6\ \mu\text{m}$  with MAMBO 1.2 mm contours overlaid. The contours are on a log scale from 30 to 440  $\text{mJy beam}^{-1}$ . Right: MIPS GAL  $24\ \mu\text{m}$  image with BGPS 1.1 mm contours. The contours are on a log scale from 0.12 to 1.1  $\text{Jy beam}^{-1}$ .

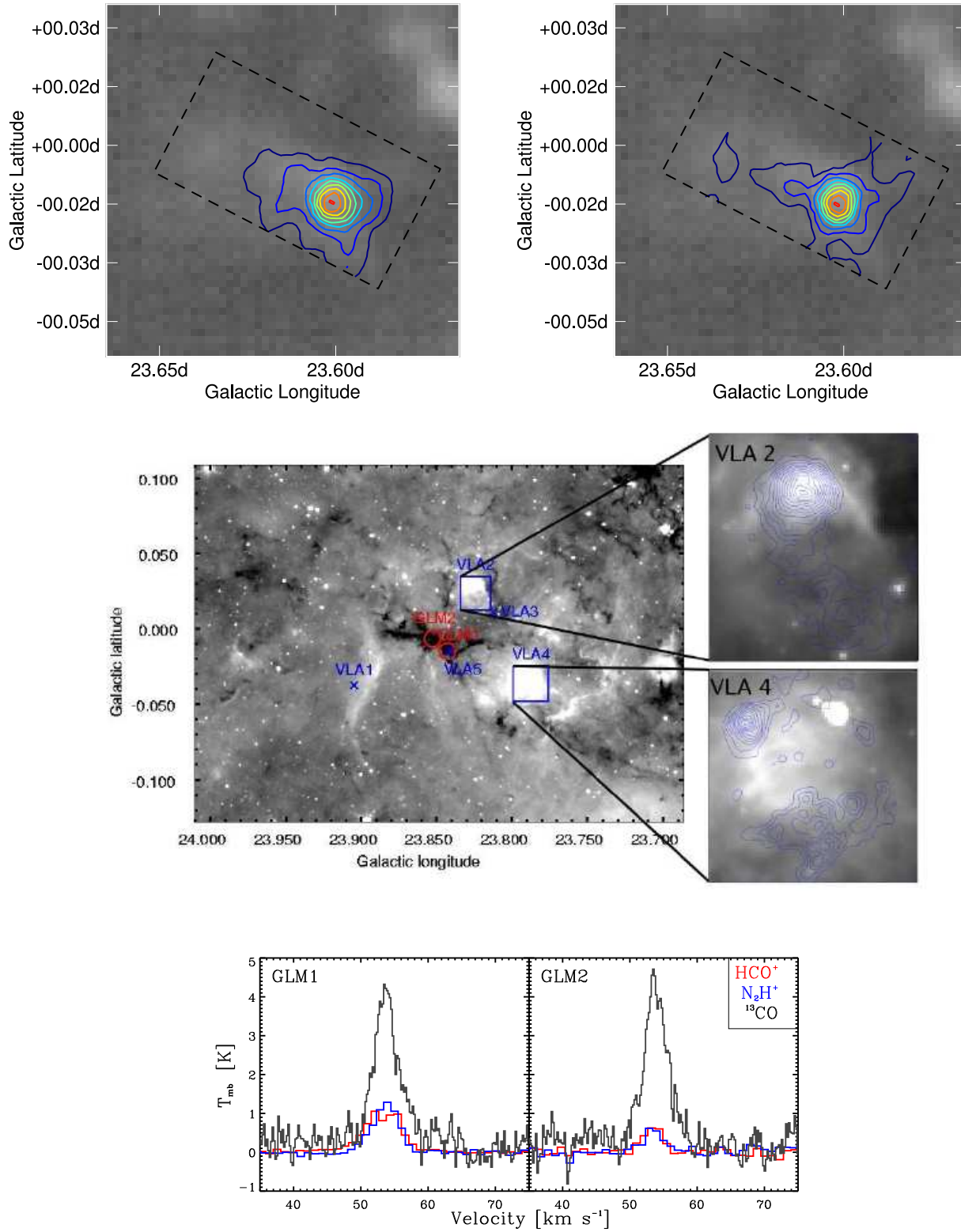


FIG. 13.— G023.60+00.00: Top Left: BGPS 1.1 mm continuum dust emission overlaid with linear HCO<sup>+</sup> contours from 1 to 10 K km s<sup>-1</sup>. Top right: BGPS 1.1 mm continuum dust emission overlaid with linear N<sub>2</sub>H<sup>+</sup> contours from 1.2 to 8.2 K km s<sup>-1</sup>. Middle: GLIMPSE 8 μm overlaid with red BGPS beam-sized apertures that were used to determine clump masses. The blue X's are VLA 3.6 cm point sources, and extended 3.6 cm sources are depicted as blue contours on the adjacent box. Right: HCO<sup>+</sup>, N<sub>2</sub>H<sup>+</sup> and <sup>13</sup>CO spectra in clumps GLM1 (Stage 3) and GLM2 (Stage 2).

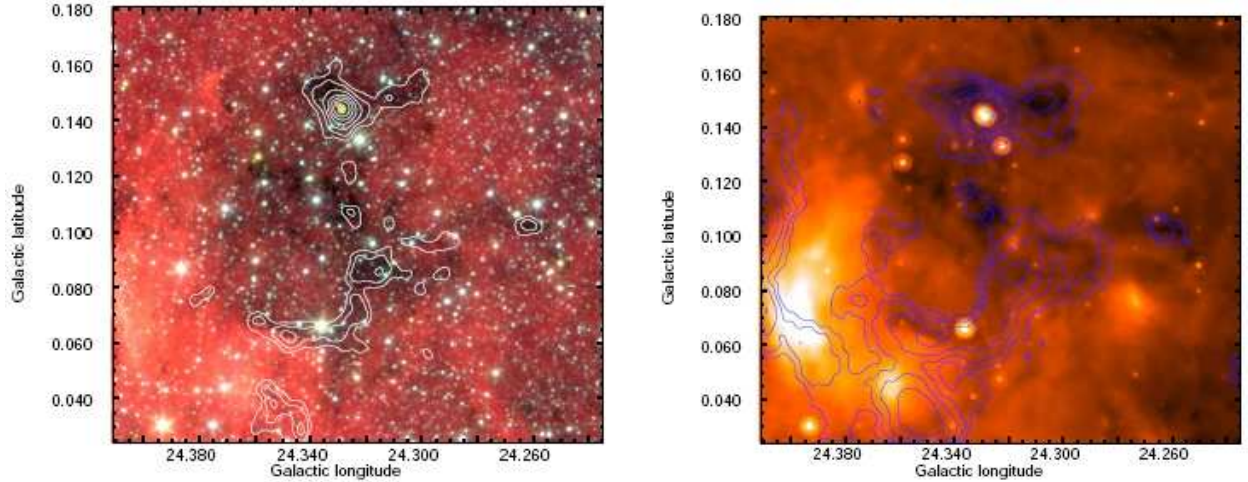


FIG. 14.— G024.33+00.11: Left: GLIMPSE three-color image, red is  $8\ \mu\text{m}$ , green is  $4.5\ \mu\text{m}$  and blue is  $3.6\ \mu\text{m}$  with MAMBO 1.2 mm contours overlaid. The contours are on a log scale from 30 to  $1280\ \text{mJy beam}^{-1}$ . Right: MIPS GAL  $24\ \mu\text{m}$  image with BGPS 1.1 mm contours. The contours are on a log scale from 0.12 to  $2.5\ \text{Jy beam}^{-1}$ .

where  $\text{HCO}^+$  and  $\text{N}_2\text{H}^+$  maps were made, they are presented as contours on a BGPS 1.1 mm greyscale image of the cloud. Also presented are the position and sizes of the apertures used for clump masses, the location of VLA 3.6 cm point sources, and where resolved, contours of 3.6 cm emission on top of a GLIMPSE  $8\ \mu\text{m}$  image. We also present  $^{13}\text{CO}$ ,  $\text{HCO}^+$ , and  $\text{N}_2\text{H}^+$  spectra at each clump position.

#### *G022.35+00.41*

G022.35+00.41 (see Figures 10 and 11) is actually composed of two clumps along the line-of-sight, one at 3.6 kpc and the other at 4.8 kpc. At least one of the two clumps is truly an active star-forming region. G022.35+00.41: GLM1 shows a bright millimeter peak, masers, a “green fuzzy,” and a  $24\ \mu\text{m}$  point source. Interferometric measurements at 1 and 3 mm on the IRAM Plateau de Bure Interferometer by Rathborne et al. (2007) show that GLM1 contains 2 cores, less than 0.026 pc each. The second clump (and associated filament) is quiescent and has diffuse millimeter emission. While the superposition of two clouds along the line-of-sight lessens the intrinsic column of either, this example shows us that in the confused inner Galaxy, it is not terribly uncommon to have two spatially coincident dense clumps.

#### *G023.60+00.00*

G023.60+00.00 (see Figures 12 and 13) is a particularly interesting example with regard to the comparison of  $8\ \mu\text{m}$  extinction and dust emission. The extinction masses of the two clumps are very close (100 and  $120\ M_\odot$ ), however, the BGPS 1.1 mm masses differ by almost a factor of two (140 and  $80\ M_\odot$ ). GLM1 is an active clump, so it is likely warmer and denser than GLM2, an intermediate clump. Also, there is a bright H II region to the southwest corner of the image shown in Figure 12, which increases the foreground  $8\ \mu\text{m}$  emission. Also, the  $\text{HCO}^+$  and  $\text{N}_2\text{H}^+$  maps show only diffuse emission around GLM2 and a bright peak toward GLM1 (see Figures 13(a) and 13(b)), tracing the dense, hot gas associated with an active clump.

At  $2.9 \times 1.8\ \text{pc}$  (major  $\times$  minor axes of the IRDC ellipse, see Figure 1), G023.60+00.00 is on the smaller side for an IRDC, and shows a filamentary morphology. It is near two evolved H II regions and a complicated web of mid-infrared bubbles, filamentary IRDCs, and Photo-Dissociation Regions (PDRs; see Figure 13(c)). The location of G023.60+00.00 is at 3.6 kpc, right amidst the active star formation in the molecular ring (Jackson et al. 2006).



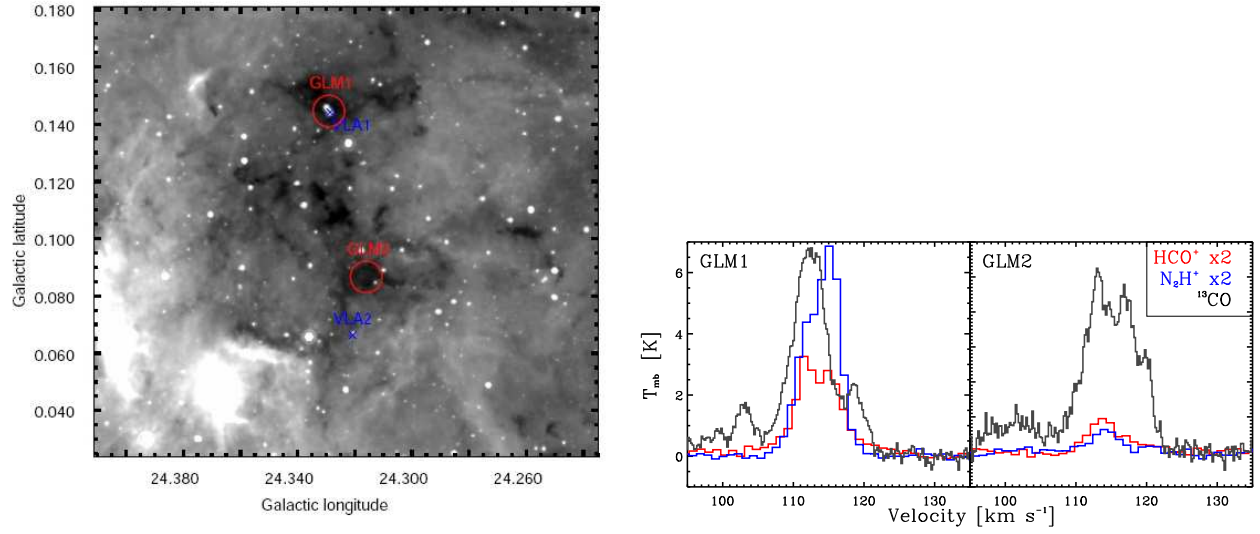


FIG. 15.— G024.33+00.11: Left: GLIMPSE  $8\ \mu\text{m}$  overlotted with red BGPS beam-sized apertures that were used to determine clump masses. The blue X's are VLA 3.6 cm point sources. Right:  $\text{HCO}^+$ ,  $\text{N}_2\text{H}^+$  and  $^{13}\text{CO}$  spectra in clumps GLM1 (Stage 3) and GLM2 (Stage 1). The  $\text{HCO}^+$  and  $\text{N}_2\text{H}^+$  spectra have been multiplied by a factor of two, in order to see them more clearly relative to the  $^{13}\text{CO}$ .

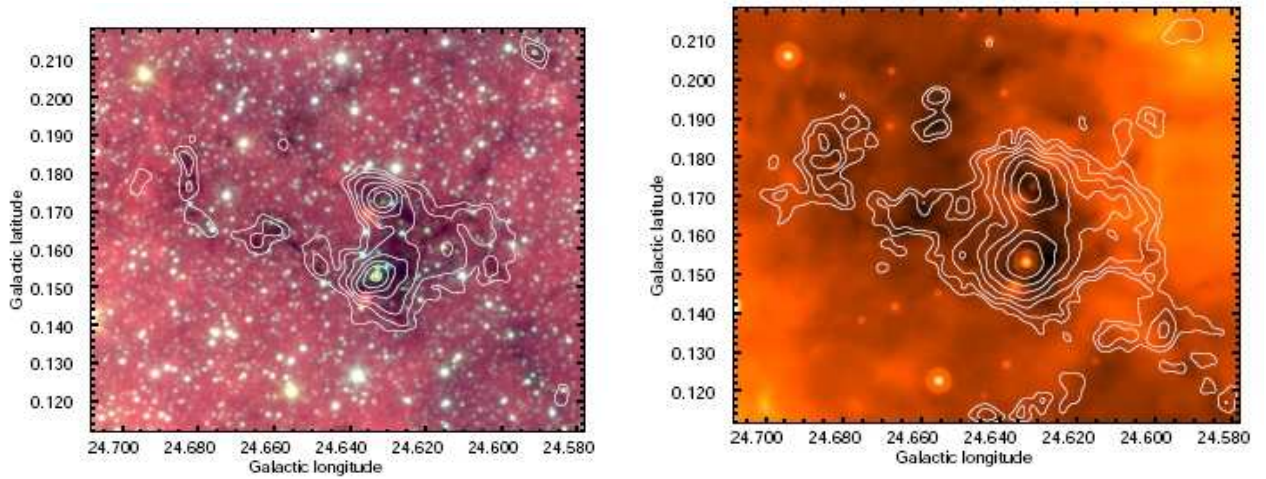


FIG. 16.— G024.60+00.08: Left: GLIMPSE three-color image, red is  $8\ \mu\text{m}$ , green is  $4.5\ \mu\text{m}$  and blue is  $3.6\ \mu\text{m}$  with MAMBO 1.2 mm contours overlaid. The contours are on a log scale from 15 to  $360\ \text{mJy beam}^{-1}$ . Right: MIPS GAL  $24\ \mu\text{m}$  image with BGPS 1.1 mm contours. The contours are on a log scale from 0.12 to  $0.8\ \text{Jy beam}^{-1}$ .

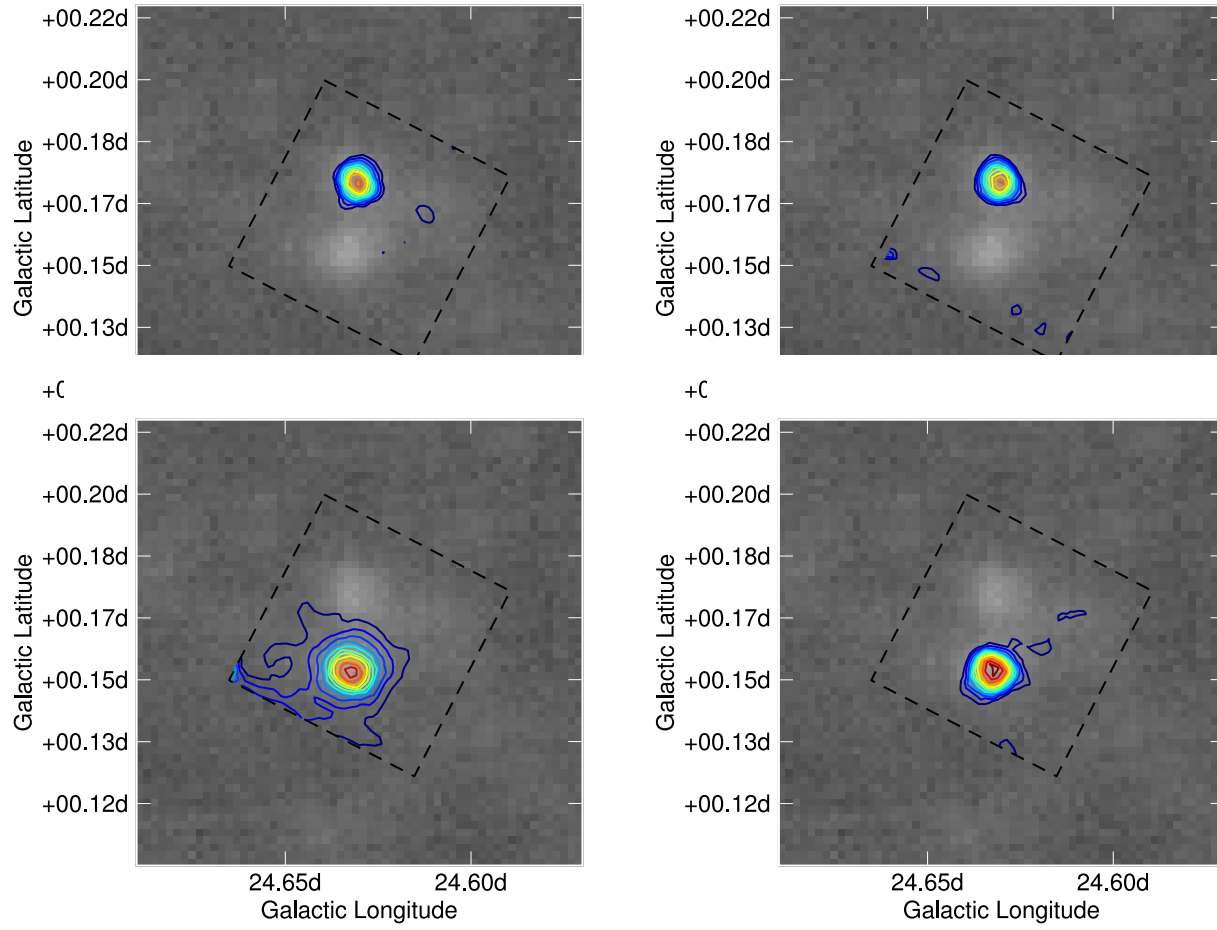


FIG. 17.— G024.60+00.08: two distinct velocity components/clumps along the line-of-sight: Top left: BGPS 1.1 mm continuum dust emission overlaid with linear  $\text{HCO}^+$  contours from 1.2 to 4.4  $\text{K km s}^{-1}$  from GLM1. Top right: BGPS 1.1 mm continuum dust emission overlaid with linear  $\text{N}_2\text{H}^+$  contours from 1.5 to 5  $\text{K km s}^{-1}$  from GLM1. Bottom left: BGPS 1.1 mm continuum dust emission overlaid with linear  $\text{HCO}^+$  contours from 1.8 to 9.8  $\text{K km s}^{-1}$  from GLM2. Bottom right: BGPS 1.1 mm continuum dust emission overlaid with linear  $\text{N}_2\text{H}^+$  contours from 1.5 to 5.5  $\text{K km s}^{-1}$  from GLM2

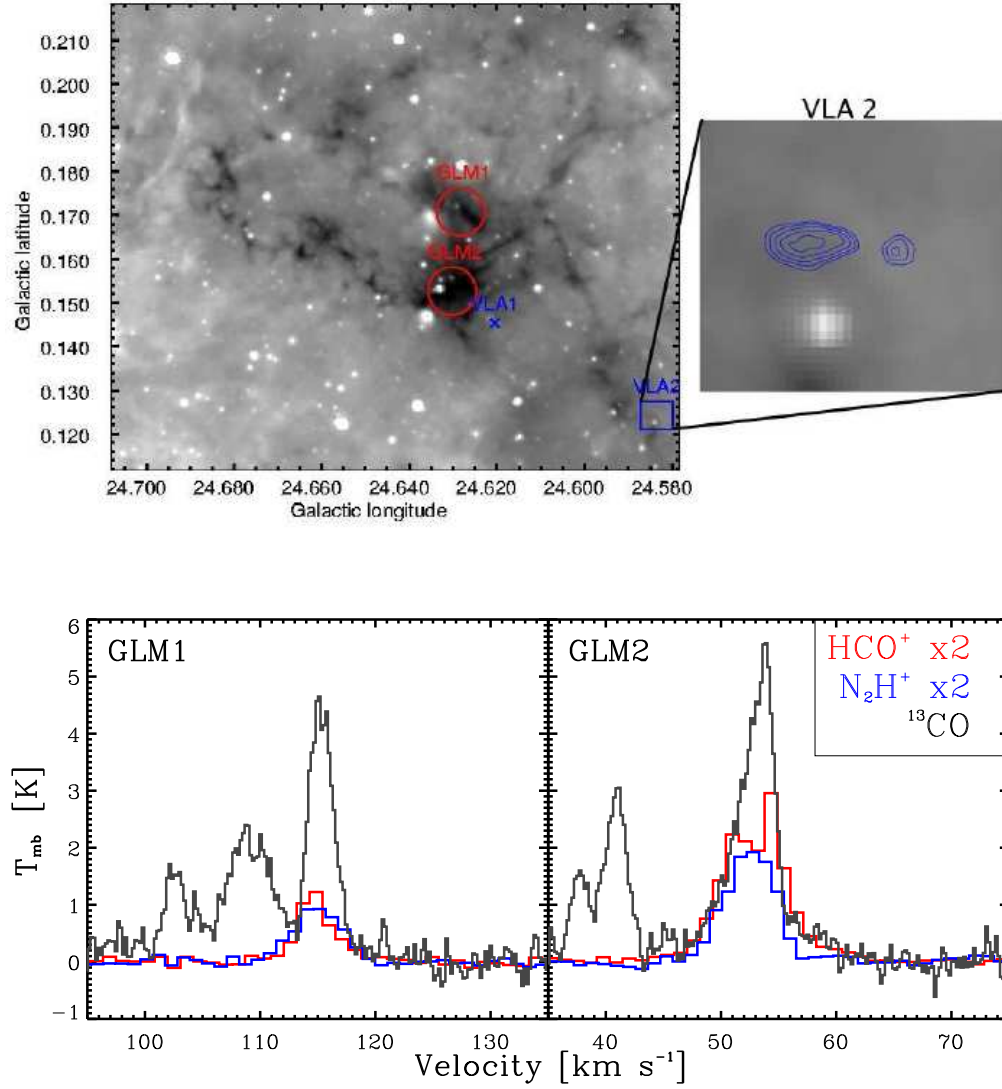


FIG. 18.— G024.60+00.08: Left: GLIMPSE 8  $\mu\text{m}$  overlaid with red BGPS beam-sized apertures that were used to determine clump masses. The blue X's are VLA 3.6 cm point sources, and extended 3.6 cm sources are depicted as blue contours in the adjacent box. Right:  $\text{HCO}^+$ ,  $\text{N}_2\text{H}^+$  and  $^{13}\text{CO}$  spectra in clumps GLM1 (Stage 2) and GLM2 (Stage 2). The  $\text{HCO}^+$  and  $\text{N}_2\text{H}^+$  spectra have been multiplied by a factor of two, in order to see them more clearly relative to the  $^{13}\text{CO}$ . Note the distinctly different clump velocities

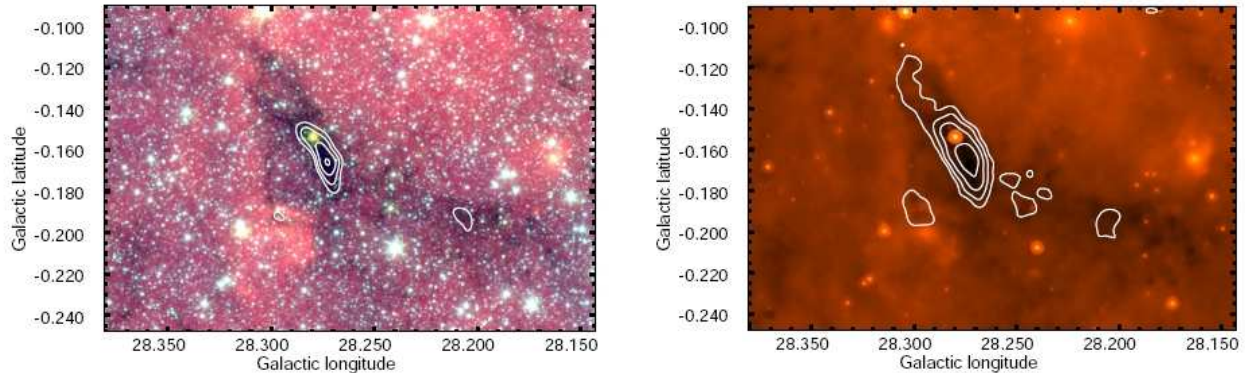


FIG. 19.— G028.23-00.19: Left: GLIMPSE three-color image, red is  $8\ \mu\text{m}$ , green is  $4.5\ \mu\text{m}$  and blue is  $3.6\ \mu\text{m}$  with MAMBO 1.2 mm contours overlaid. The contours are on a log scale from 30 to  $112\ \text{mJy beam}^{-1}$ . Right: MIPSGAL  $24\ \mu\text{m}$  image with BGPS 1.1 mm contours. The contours are on a log scale from 0.12 to  $0.64\ \text{Jy beam}^{-1}$ .

#### *G024.33+00.11*

G024.33+00.11 (see Figures 14 and 15) contains a dense, active clump and more diffuse filamentary structure. There is a ridge between dark  $8\ \mu\text{m}$  extinction and bright  $8\ \mu\text{m}$  emission at the southern edge of the cloud. At a distance of 5.9 kpc, this cloud is among the most distant in our sample. G024.33+00.11 was not mapped in  $\text{HCO}^+$  and  $\text{N}_2\text{H}^+$ , but it would be a good candidate for a future mapping project, to see if the dense ridge is associated with the IRDC. Additionally, portions of the cloud are dark at  $8\ \mu\text{m}$ , but show very little millimeter emission.

G024.33+00.11: GLM1 is a particularly good example of a dense, active clump. Interferometric measurements at 1 and 3 mm on the IRAM Plateau de Bure Interferometer by Rathborne et al. (2007) show that G024.33+00.11: GLM1 has a single core smaller than 0.035 pc. Figure 15(b) exemplifies the increase of  $\text{HCO}^+$  and  $\text{N}_2\text{H}^+$  in an active clump, and the self-absorption of  $^{13}\text{CO}$  and  $\text{HCO}^+$  in a particularly dense environment. This is in contrast to the weak  $\text{HCO}^+$  and  $\text{N}_2\text{H}^+$  detections in G024.33+00.11: GLM2.

#### *G024.60+00.08*

G024.60+00.08 (see Figures 16, 17, and 18) is the second (of two) examples in our sample which is comprised of two unique clumps along the line-of-sight, rather than one contiguous object. The two clumps are spatially adjacent with only a slight overlap of diffuse emission, which is an astonishing coincidence. The  $\text{HCO}^+$  and  $\text{N}_2\text{H}^+$  maps confirm (see Figure 17) this chance alignment.

At 6.0 kpc, G024.60+00.08: GLM1 is the most distant clump in our sample. The  $8\ \mu\text{m}$  extinction does not appear abnormally large, but given the amount of foreground emission between us and the clump, it has one of the highest extinction masses in our sample. G024.60+00.08: GLM2, on the other hand, is located in the molecular ring at 3.4 kpc. This clump shows self-absorption of  $\text{HCO}^+$ , and an asymmetric line profile in  $^{13}\text{CO}$ , indicative of outflows. These clumps are both categorized as intermediate. Interferometric measurements at 1 and 3 mm on the IRAM Plateau de Bure Interferometer by Rathborne et al. (2007) show that G024.60+00.08: GLM1 contains 5 cores, less than 0.041 pc each, while GLM2 contains 3 cores, smaller than 0.024 pc each.

#### *G028.23-00.19*

G028.23-00.19: GLM1 (see Figures 19 and 20) is the prime example of a starless IRDC clump. It is typical of an IRDC clump in size, mass,  $8\ \mu\text{m}$  extinction, and in having a relatively compact millimeter core. However, this clump has absolutely no signs of star formation. The detections of  $\text{HCO}^+$  and  $\text{N}_2\text{H}^+$  in this source are incredibly weak. The dust column is comparable to many other clumps with bright  $\text{HCO}^+$  and  $\text{N}_2\text{H}^+$ , the primary difference being the lack of density and a heating source in G028.23-00.19: GLM1. The  $8\ \mu\text{m}$  point source just north of GLM1 may be an indication of nearby, recent star formation. Given the compact nature of GLM1, its high column density, and nearby star formation, it seems likely that it is a quiescent precursor to massive star formation.

#### *G028.37+00.07*

G028.37+00.07 (see Figures 21 and 22) is an extremely varied cloud. It was identified by Simon et al. (2006a) as the darkest (by contrast) cloud in the First Galactic quadrant. Due to a particularly bright background around the cloud at  $8\ \mu\text{m}$  (as discussed in §3.2) the extinction column density is over-estimated as compared with the BGPS 1.1 mm column density. This cloud is the most massive (by all tracers) in our sample. G028.37+00.07 is composed of dense filaments and surrounded by an extremely bright mid-IR background, including nearby evolved H II regions.

G028.37+00.07 hosts a prime example of a “diffuse red clump.” In Figure 21(a), we see a “diffuse red clump,” spatially separated from the bright millimeter peak. The H II region producing this “red” clump is asymmetric. Away from the millimeter clump, the H II region has expanded and become more diffuse and toward the millimeter clump the H II region remains confined by the high-density.

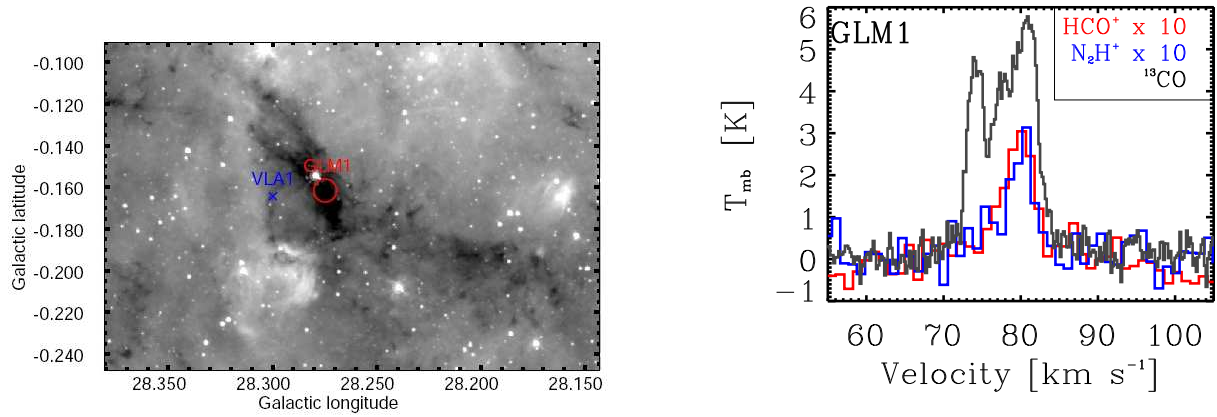


FIG. 20.— G028.23-00.19: Left: GLIMPSE  $8\ \mu\text{m}$  overlaid with red BGPS beam-sized aperture that was used to determine the clump mass. The blue X's are VLA 3.6 cm point sources. Right:  $\text{HCO}^+$ ,  $\text{N}_2\text{H}^+$  and  $^{13}\text{CO}$  spectra in clump GLM1 (Stage 1). The  $\text{HCO}^+$  and  $\text{N}_2\text{H}^+$  spectra have been multiplied by a factor of ten, in order to see them more clearly relative to the  $^{13}\text{CO}$ .

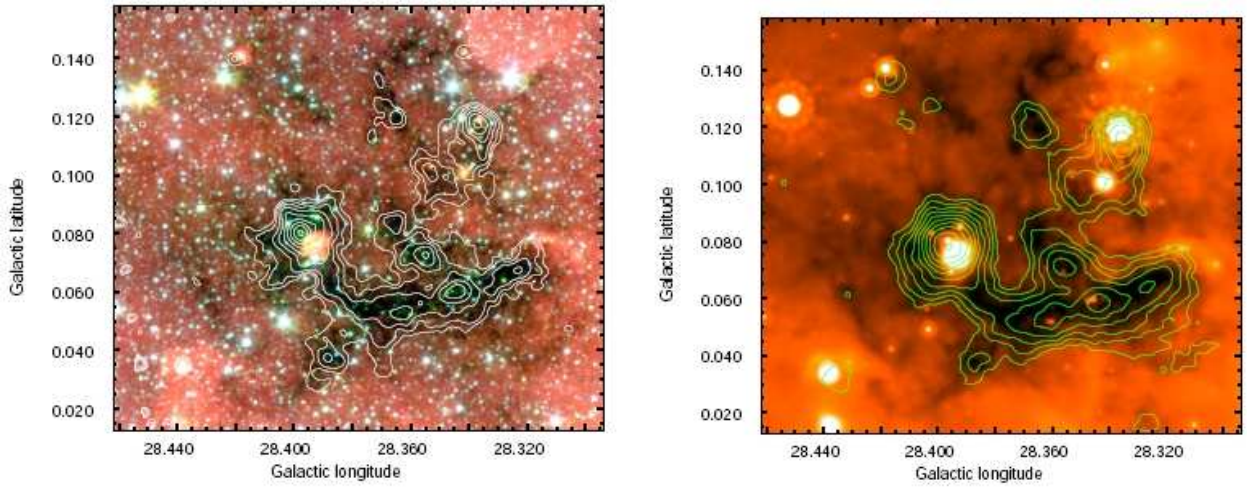


FIG. 21.— G028.37+00.07: Left: GLIMPSE three-color image, red is  $8\ \mu\text{m}$ , green is  $4.5\ \mu\text{m}$  and blue is  $3.6\ \mu\text{m}$  with MAMBO 1.2 mm contours overlaid. The contours are on a log scale from 30 to 1340 mJy beam $^{-1}$ . Right: MIPS GAL  $24\ \mu\text{m}$  image with BGPS 1.1 mm contours. The contours are on a log scale from 0.2 to 2.2 Jy beam $^{-1}$ .

The structure of  $\text{HCO}^+$  and  $\text{N}_2\text{H}^+$  in G028.37+00.07 is a great example of the differing ratio of  $\text{HCO}^+/\text{N}_2\text{H}^+$ . The  $\text{HCO}^+$  and  $\text{N}_2\text{H}^+$  maps show a similar overall structure, but the intensities of the two tracers vary across different clumps. In  $\text{HCO}^+$ , GLM2 is the brightest, and in  $\text{N}_2\text{H}^+$ , GLM4 is by far the brightest. As pointed out previously, however, this is not due to chemical differentiation. Rather, the  $\text{HCO}^+$  and even the  $\text{N}_2\text{H}^+$  become optically thick (and self-absorbed) in the densest clump, GLM4. The self-absorption of  $\text{HCO}^+$  makes  $\text{N}_2\text{H}^+$  appear brighter by comparison.

Wang et al. (2008) and Zhang et al. (2009) observed G028.37+00.07: GLM2 and GLM4 (referred to as P1 and P2) with the VLA and SMA, respectively. In GLM2, they find 5 cores along the filament with line widths of about  $1.2\ \text{km s}^{-1}$  and temperature of about 15 K. In GLM4, they find 2 cores with line widths of about  $4.3\ \text{km s}^{-1}$ , temperatures of about 30 K, and a rich molecular spectra.

#### G028.53-00.25

G028.53-00.25 (see Figures 23 and 24) is a curious example of a source with a very small extinction column as compared with the BGPS 1.1 mm column. This cloud either has an exceptionally low background or high foreground. The region surrounding G028.53-00.25 is mostly devoid of extended H II regions, PDRs, and other strong emitters of diffuse  $8\ \mu\text{m}$  emission. Due to the paucity of nearby diffuse  $8\ \mu\text{m}$  emission, the background estimate is decreased, and the extinction column estimate too low.

G028.53-00.25 is a fairly quiescent cloud with few indicators of star formation. The clump, GLM1, is identified as intermediate due to the presence of a “green fuzzy” (though a fairly compact, faint one) and  $24\ \mu\text{m}$  point source. GLM1 shows very weak  $\text{HCO}^+$  and  $\text{N}_2\text{H}^+$  emission (the OTF-maps suffer from low signal to noise). G028.53-00.25: GLM1

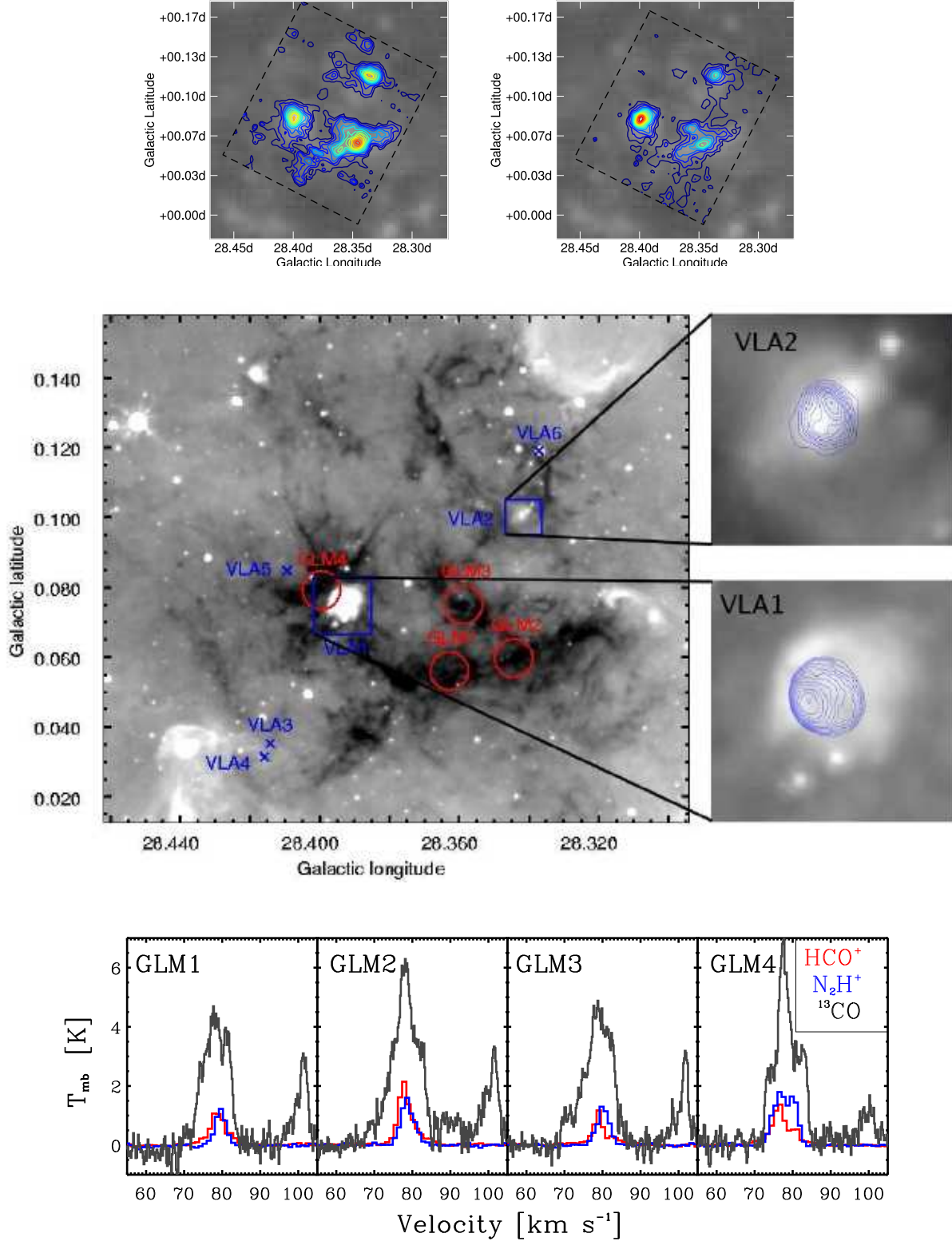


FIG. 22.— G028.37+00.07: Top left: BGPS 1.1 mm continuum dust emission overlaid with linear  $\text{HCO}^+$  contours from 1.2 to 9 K km s $^{-1}$ . Top right: BGPS 1.1 mm continuum dust emission overlaid with linear  $\text{N}_2\text{H}^+$  contours from 0.8 to 10 K km s $^{-1}$ . Middle: GLIMPSE  $8\ \mu\text{m}$  overlaid with the BGPS beam-sized apertures that were used to determine clump masses. The blue X's are VLA 3.6 cm point sources, and extended 3.6 cm sources are depicted as blue contours in the adjacent boxes. Right:  $\text{HCO}^+$ ,  $\text{N}_2\text{H}^+$  and  $^{13}\text{CO}$  spectra in clumps GLM1 (Stage 1), GLM2 (Stage 2), GLM3 (Stage 2), and GLM4 (Stage 2, slightly overlapping with Stage 4 “diffuse red clump”).

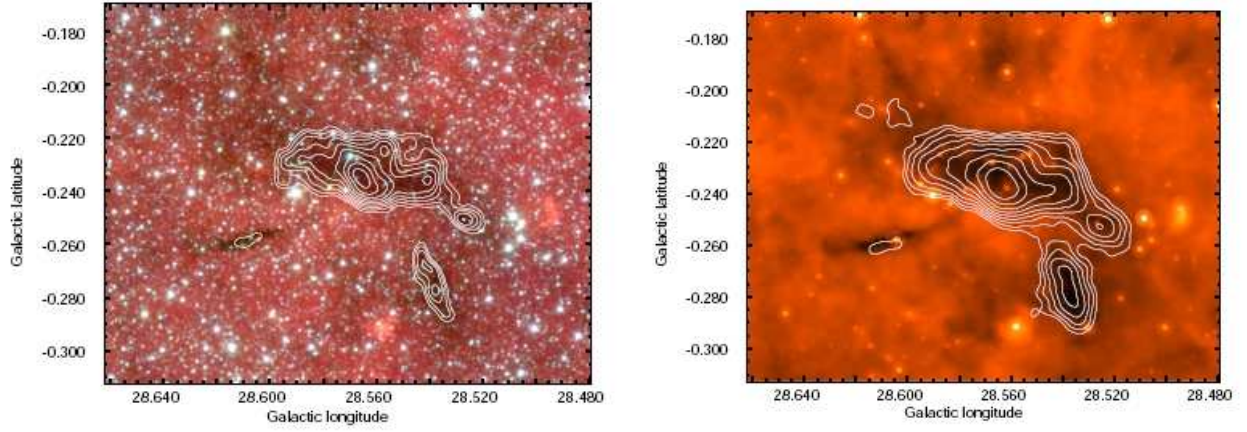


FIG. 23.— G028.53-00.25: Left: GLIMPSE three-color image, red is  $8 \mu\text{m}$ , green is  $4.5 \mu\text{m}$  and blue is  $3.6 \mu\text{m}$  with MAMBO 1.2 mm contours overlaid. The contours are on a log scale from 30 to  $320 \text{ mJy beam}^{-1}$ . Right: MIPS GAL  $24 \mu\text{m}$  image with BGPS 1.1 mm contours. The contours are on a log scale from 0.12 to  $1.3 \text{ Jy beam}^{-1}$ .

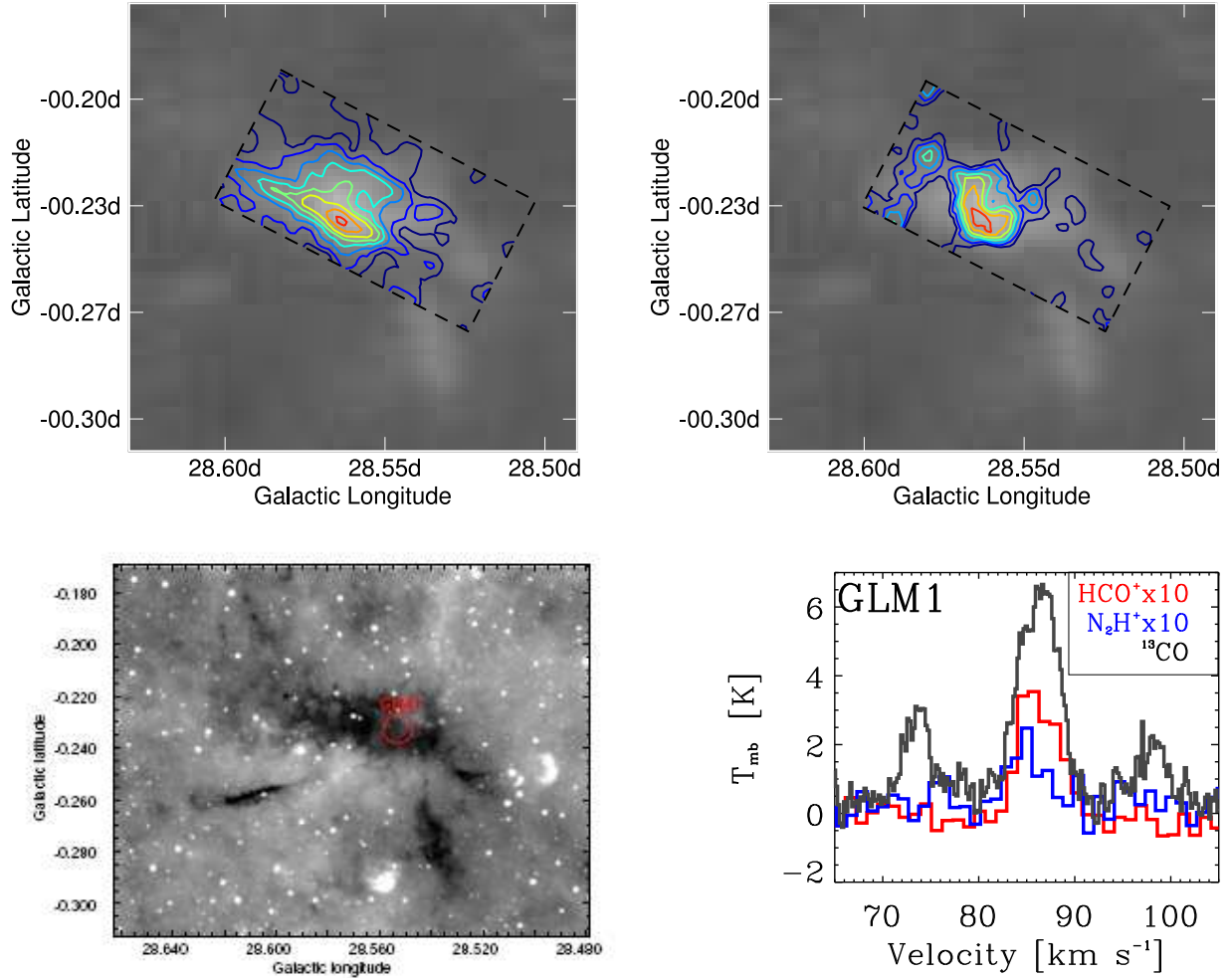


FIG. 24.— G028.53-00.25: Top left: BGPS 1.1 mm continuum dust emission overlaid with linear  $\text{HCO}^+$  contours from  $0.43$  to  $7 \text{ K km s}^{-1}$ . Top right: BGPS 1.1 mm continuum dust emission overlaid with linear  $\text{N}_2\text{H}^+$  contours from  $0.9$  to  $3.6 \text{ K km s}^{-1}$ . Bottom left: GLIMPSE  $8 \mu\text{m}$  overlaid with red BGPS beam-sized apertures that were used to determine clump masses. Bottom right:  $\text{HCO}^+$ ,  $\text{N}_2\text{H}^+$  and  $^{13}\text{CO}$  spectra in clump GLM1 (Stage 2). The  $\text{HCO}^+$  and  $\text{N}_2\text{H}^+$  spectra have been multiplied by a factor of ten, in order to see them more clearly relative to the  $^{13}\text{CO}$ .

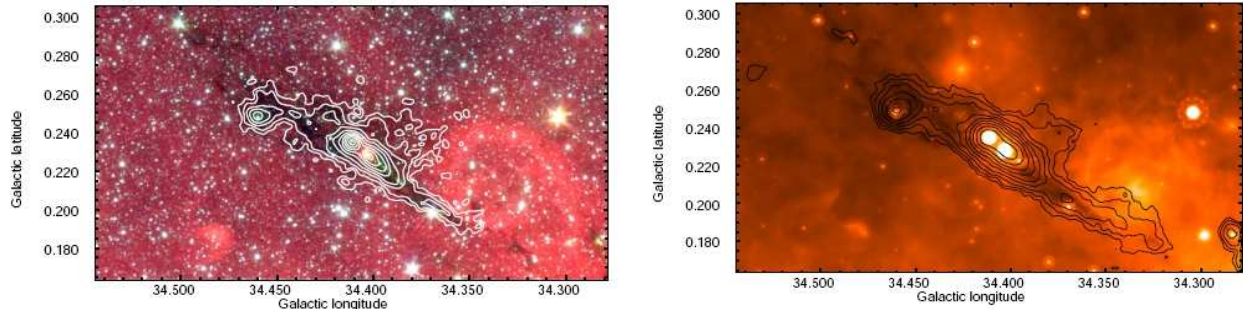


FIG. 25.— G034.43+00.24: Left: GLIMPSE three-color image, red is  $8\ \mu\text{m}$ , green is  $4.5\ \mu\text{m}$  and blue is  $3.6\ \mu\text{m}$  with MAMBO 1.2 mm contours overlaid. The contours are on a log scale from 30 to  $2400\ \text{mJy beam}^{-1}$ . Right: MIPS GAL  $24\ \mu\text{m}$  image with BGPS 1.1 mm contours. The contours are on a log scale from 0.12 to  $4.3\ \text{Jy beam}^{-1}$ .

was observed on the Submillimeter Array by Rathborne et al. (2008) who found that GLM1 contains at least three compact (less than  $\sim 0.06\ \text{pc}$ ) cores. This quiescent cloud could be the host of low mass star formation, or it could be a transient density enhancement or a quiescent proto-cluster.

#### *G034.43+00.24*

G034.43+00.24 (see Figures 25 and 26) is a stunning example of an active IRDC. This object is just northeast of the enormously bright H II region at G34.3+0.2, RH85 (Reid & Ho 1985). This complex contains the bright H II region, RH85, and the shells of supernova remnants. G034.43+00.24, along with a few other IRDCs not discussed in the paper, are extremely filamentary structures, streaming radially out of this bright H II region complex, increasing in width with distance from the complex. This is an excellent source in which to study the triggered formation mechanism of IRDCs (e.g Redman et al. 2003).

South of G034.43+00.24: GLM2 is long train of “green fuzzies,” along the IRDC. Rathborne et al. (2008) observed G034.43+00.24: GLM1 with the Submillimeter Array and found that GLM1 remains unresolved and contains a core smaller than the  $\sim 0.03\ \text{pc beam}$ . GLM2 itself is an excellent example of a “diffuse red clump,” offset from the millimeter peak. The bright  $8\ \mu\text{m}$  emission nullifies the use of an extinction mass in this clump; the extinction mass is  $60\ M_{\odot}$  while the BGPS 1.1 mm mass is  $780\ M_{\odot}$ . This clump is one of the most “massive” sources in our sample according to the BGPS 1.1 mm mass, which is almost certainly biased by a higher dust temperature than the assumed 15 K. This spectacular clump is an example where all of our conventional mass tracers fail. The  $\text{HCO}^+$  and  $\text{N}_2\text{H}^+$  are extremely bright in all the clumps, especially GLM1 and GLM2 (the brightest by far in our sample). There is also strong self-absorption in  $^{13}\text{CO}$  toward these clumps, further indication of the high density and temperatures of these active clumps.



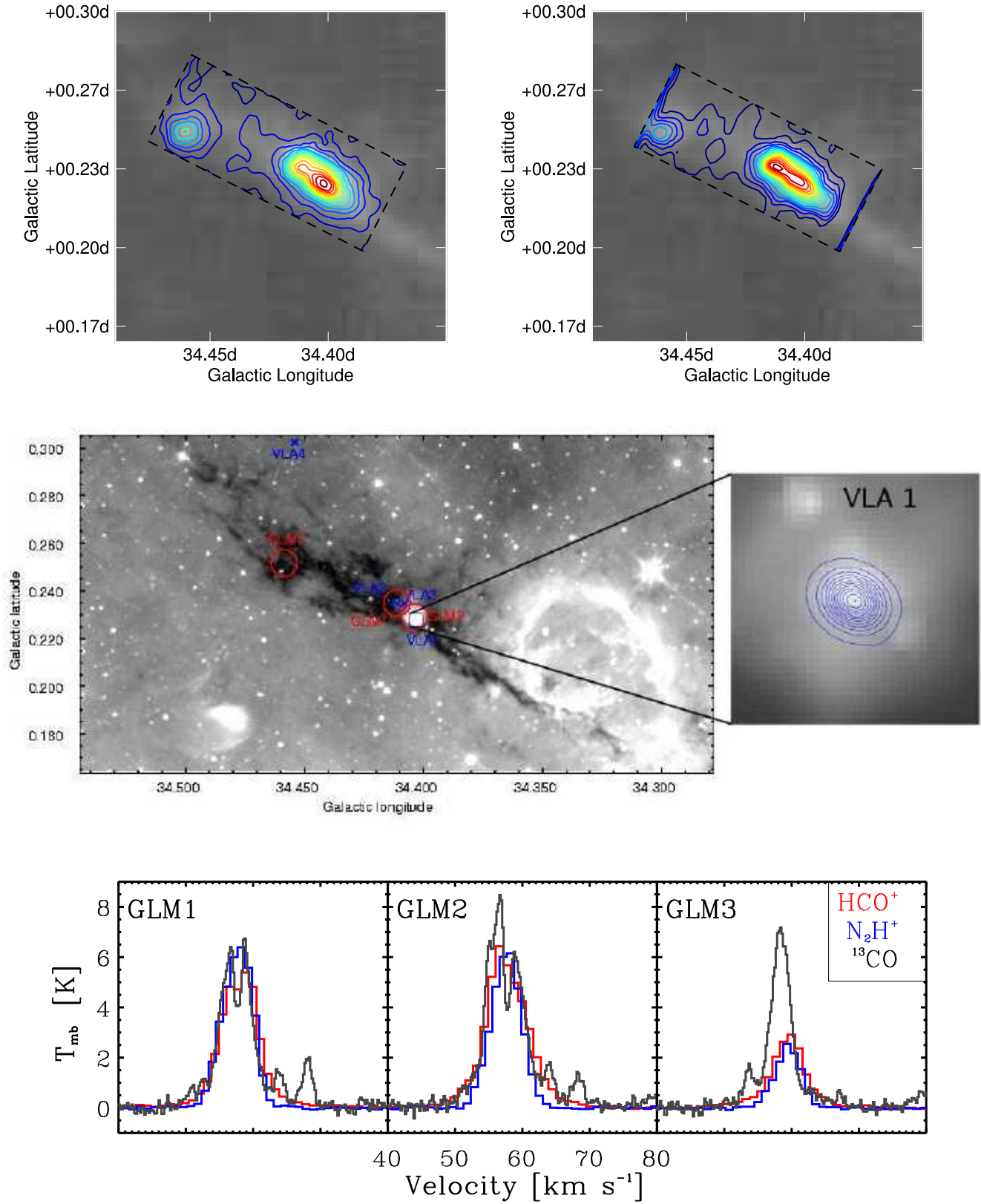


FIG. 26.— G034.43+00.24: Top left: BGPS 1.1 mm continuum dust emission overlaid with linear  $\text{HCO}^+$  contours from 0.55 to 38  $\text{K km s}^{-1}$ . Top right: BGPS 1.1 mm continuum dust emission overlaid with linear  $\text{N}_2\text{H}^+$  contours from 0.48 to 27  $\text{K km s}^{-1}$ . Middle: GLIMPSE 8  $\mu\text{m}$  overlaid with the BGPS beam-sized apertures that were used to determine clump masses. The blue X's are VLA 3.6 cm point sources, and extended 3.6 cm sources are depicted as blue contours in the adjacent box. Right:  $\text{HCO}^+$ ,  $\text{N}_2\text{H}^+$  and  $^{13}\text{CO}$  spectra in clumps GLM1 (Stage 3), GLM2 (Stage 4), and GLM3 (Stage 2).

